



Contents lists available at ScienceDirect

Comput. Methods Appl. Mech. Engrg.

journal homepage: www.elsevier.com/locate/cma

The inverse medium problem in heterogeneous PML-truncated domains using scalar probing waves

Jun Won Kang, Loukas F. Kallivokas*

Department of Civil, Architectural and Environmental Engineering, The University of Texas at Austin, 1 University Station, C1748, Austin, TX 78712, USA

ARTICLE INFO

Article history:

Received 2 February 2010
Received in revised form 19 July 2010
Accepted 19 August 2010
Available online 21 September 2010

Keywords:

Inverse medium problem
Full waveform inversion
Perfectly-matched-layer (PML)
Mixed unsplit-field formulation
PDE-constrained optimization
Marmousi model

ABSTRACT

We discuss the inverse medium problem associated with semi-infinite domains. In particular, we attempt to image the spatial variability of shear moduli or shear wave velocities from scant surficial measurements of an arbitrarily heterogeneous semi-infinite domain's response to prescribed dynamic excitations.

We use a full waveform approach to drive the inversion process, within a PDE-constrained optimization framework. Due to the semi-infinite extent of the targeted domains, we introduce perfectly-matched-layers (PMLs) to arrive at finite computational domains. The numerical implementation is based on a mixed finite-element method that is used to resolve the ensuing state and adjoint boundary-value problems, both of which are PML-endowed. To alleviate the inherent solution multiplicity, we use Tikhonov and total variation (TV) regularization schemes, in conjunction with a regularization factor continuation scheme. To further improve the optimizer's chances to converge, we also discuss a source-frequency continuation scheme.

We report on two-dimensional numerical experiments using synthetic data. Included are layered profiles, and profiles involving inclined layers and inclusions. We also report on our methodology's reconstruction of the highly-heterogeneous Marmousi benchmark velocity model.

© 2010 Elsevier B.V. All rights reserved.

1. Introduction

Subsurface imaging aims at reconstructing the material profile of a domain of interest in terms of, for example, elastic modulus, or shear wave velocity, when given surficial measurements of the response of the probed domain to interrogating waves. The problem arises predominantly in geotechnical site characterization and geophysical probing applications, but shares a common thread with many other non-invasive condition assessment processes. In this article, we focus on a particular class of the subsurface imaging applications: we discuss a systematic methodology and associated numerical results for reconstructing the shear wave velocity profile in a two-dimensional heterogeneous elastic soil medium of semi-infinite extent. Waves are used to probe the stratigraphy, realized via applied excitations on the soil's surface, and the response is recorded directly in the time-domain at a few stations also situated on the surface. The recorded response is then used to drive the imaging of the probed domain.

Mathematically, the problem entails the identification of the spatially dependent coefficients of the (two-dimensional) hyperbolic partial differential equation (PDE) governing the physics of

the problem (wave equation). The PDE coefficients may be either continuous, or piecewise continuous. The problem is often referred to as the inverse medium problem, for it is through knowledge of the source terms (loads) and the medium's response that one seeks to recover the medium's properties.

We address two primary issues associated with the inverse medium problem. First, in order to limit the semi-infinite extent of the physical domain, perfectly-matched-layers (PMLs) are introduced at truncation interfaces to render the domain finite. This is a critical step, particularly for near-surface investigations, which is oftentimes ignored or grossly simplified in applications due to the complexity associated with truncation boundaries. However, the inaccurate or inadequate modeling of truncation boundaries stands to introduce reflections in the finite domain that, in turn, stand to distort the inverted profiles. Secondly, we discuss a systematic waveform inversion approach for recovering the spatial variation of the soil's shear wave velocity.

On the first issue, the fundamental strategy is to truncate the semi-infinite extent of the physical domain by introducing a wave absorbing buffer region within which the waves are forced to artificially decay. Among such absorbing buffers, the PML is the most widely used scheme, since it has been shown to absorb outgoing waves without generating reflections for all frequencies and angles of incidence other than grazing [1,2]. Transparent conditions are alternative ways of dealing with the truncation surface; they can

* Corresponding author.

E-mail addresses: jwkang@mail.utexas.edu (J.W. Kang), loukas@mail.utexas.edu (L.F. Kallivokas).

be broadly classified as either local [3–5], or non-local [6,7]. Transparent conditions allow the passage of waves with, ideally, no or minimal reflections from the interface. However, they are typically constructed based on the rather constraining assumption of a homogeneous exterior domain (the part of the domain that will be excluded from subsequent computations), which is seldom the case in realistic settings. By contrast, PMLs do not suffer from this limitation, and are better able to handle heterogeneity. Thus, in this work, we favor PMLs, and discuss the casting of the inverse problem over a finite computational domain using PMLs on the truncation boundaries.

Direct time-domain PML developments, which are of interest herein, could be roughly classified as approaches based on split-field (e.g. [1,2,12]), and unsplit-field schemes (e.g. [8–10]). However, none of the prior developments could be easily integrated within a PDE-constrained optimization framework, which we favor herein for dealing with the inverse problem. Specifically, the difficulty with past PML developments arises with adjoint formulations, and prevents a systematic treatment. Motivated by this need, we have recently developed ([11]) a new mixed unsplit-field PML approach for one-dimensional elastic, and two-dimensional SH waves, which we adopt here for modeling the wave motion.

The second key technical issue is the systematic treatment of the inverse problem. The interest here is to exploit the information embedded in the *complete* waveforms, typically recorded directly in the time-domain and on the probed domain's surface: use of the complete record gives rise to a full waveform inversion approach. In the last thirty years, waveform inversion, in general, has been intensely pursued in many technical areas (e.g. medical imaging, non-destructive testing, oil-exploration, etc.), in both the frequency-domain [13], and the time-domain [14,15], owing to the significance of the underlying applications. For example, Pratt and Shipp [16], Operto et al. [15], Gao et al. [17], and Choi et al. [18,19] explored full waveform inversion using either real or synthetic data sets to reconstruct complicated earth velocity structures (e.g. the Marmousi profile). In general, waveform-based inversion approaches could be divided into either migration velocity analysis (MVA) approaches [26–28], or full waveform-based schemes (see [43] for a short overview). In a recent comprehensive discussion of MVA [42], Symes has highlighted advantages of MVA over full waveform approaches, whose robustness appears sensitive to the initial profile guess. On the other hand, MVA requires decomposition of the sought properties into the, so-called, background and reflectivity components, followed by a rather complex forward modeling (a two-step process involving prestack migration and a standard forward solution), and a fairly expensive optimization procedure for recovering the reflectivity. Full waveform approaches are not without disadvantages either: the presence of multiple minima and their treatment, of which the initial guess sensitivity is only one manifestation, remains an open problem. However, advances in both computer architecture and optimization algorithms have already enabled large-scale three-dimensional full waveform inversion in acoustic and elastic media using synthetic data [20,21]. Strategies to alleviate the inherent ill-posedness, in order to lend algorithmic robustness to full waveform approaches, continue to be refined, and could be roughly classified into direct regularization approaches (e.g. Tikhonov [30]), and continuation schemes (e.g. [21,41]). In the absence of a definitive choice to date, here we opted for a full waveform approach, similar to the recent work by Epanomeritakis et al. [21]. The key conceptual difference between their work and what we discuss here is the adoption of a PML as the truncation condition, which, in turn, adds complexity in both the forward and the inverse modeling. Similar to [21] we use a full waveform approach embedded within a PDE-constrained optimization framework. However, the introduction of the PML results in a mixed formulation with dis-

placements and stress memories as unknowns, unlike the formulation in [21] where local transparent conditions led to a displacement-only formulation (of course, the problem treated in [21] has other significant complexities of its own, not present in the problem we are treating, owing to the three spatial dimensions, and the presence of two wave velocities). The acoustic (or SH) wave case of interest herein has been treated earlier using a similar approach, first in fullspace (3D) [22], where, however, sensors and receivers were used to completely circumscribe the probed domain as is typically the case in medical imaging, and later in halfplanes (2D) [23–25], using, however, simple local transparent boundaries to truncate the semi-infinite extent of the domain. The primary enhancement this work provides over the preceding developments is the incorporation of a physically-consistent treatment of the truncation interface in the presence of heterogeneity: in geophysical probing applications over very large length scales, the introduction of a PML may not be critical, but it is fairly important in seismic inversion applications and, more so, in geotechnical site characterization applications, where the high-fidelity reconstruction of near-surface heterogeneous deposits is of significance.

We also discuss both Tikhonov and total variation regularization schemes to help alleviate solution multiplicity. We present a regularization factor continuation scheme, which renders flexibility in the choice of the regularization factor, and results in a modest iteration speed-up. To improve on the optimizer's chances to converge, we also discuss a source-frequency continuation scheme, whereby we expose the probed domain to multiple illuminations.

We report several numerical experiments that lead efficiently to the reconstruction of heterogeneous shear wave velocity profiles involving both horizontal and curved layers, as well as of profiles involving inclusions within layered systems. We use both noise-free and noisy data, and report on the reconstructed profiles. Lastly, we discuss our experience in reconstructing the Marmousi benchmark velocity model.

2. Forward modeling in a 2D PML-truncated domain

Consider a heterogeneous semi-infinite soil medium as shown in Fig. 1(a) (the medium need not be necessarily layered). We are interested in scalar waves (SH) traveling in the soil when a stress load $p(t)$ is applied on the surface. In this setting, the scalar wave motion is governed by the two-dimensional wave equation:

$$\nabla \cdot (\mu \nabla u) = \rho \frac{\partial^2 u}{\partial t^2}, \quad (1)$$

where u is anti-plane displacement, ρ is density, and μ denotes the shear modulus of the host medium. Similar problems arise if one were to consider pressure waves in an acoustic domain. To solve (1) within a domain of semi-infinite extent (Fig. 1(a)), we truncate the domain, attach PMLs on the truncation boundaries of the now finite computational domain of interest, and enforce the attenuation of the outgoing waves within the PMLs. Fig. 1(b) depicts the truncated computational domain (Ω_{Regular}) surrounded by the PMLs (Ω_{PML}). Without loss of generality, let the x_1 axis coincide with the horizontal surface of the original semi-infinite domain, and let the x_2 axis be an axis of symmetry of the $\Omega = \Omega_{\text{Regular}} \cup \Omega_{\text{PML}}$ domain.

In [11], we discussed a mixed displacement-stress memory formulation that, starting from the standard wave Eq. (1), leads to a system of coupled PDEs in the time-domain. The solution of the system captures accurately the wave motion within the regular domain, while simultaneously enforcing rapid motion attenuation within the PML buffer zone. Here, we repeat for completeness, the main ingredients of the mixed approach to the forward modeling problem. Much of the development hinges on a complex-coordinate stretching concept, by which the wave attenuation is

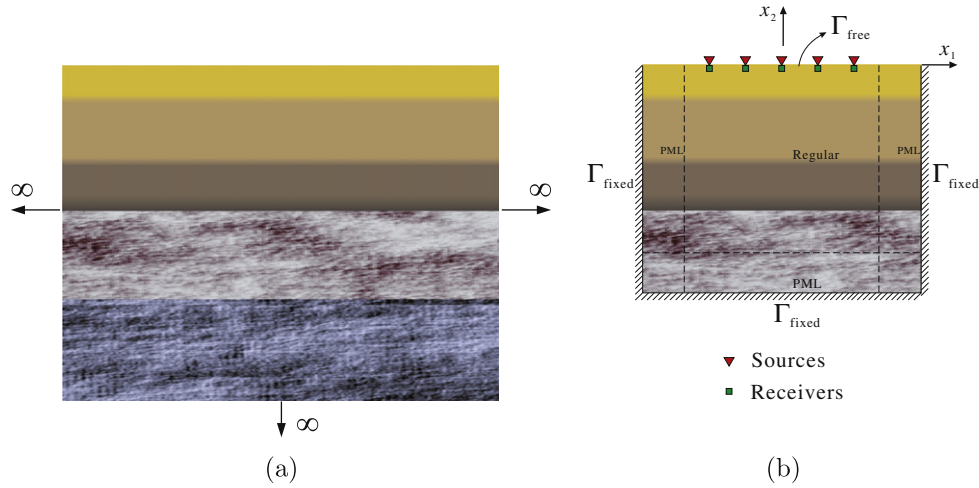


Fig. 1. (a) A semi-infinite soil domain; (b) conceptual configuration of a PML-truncated semi-infinite soil domain in two-dimensions.

enforced within the PML. Accordingly, the physical coordinate $x_j (j = 1, 2)$, is “stretched” to become [9–11]:

$$\tilde{x}_j = \int_0^{x_j} \left[\left\{ 1 + f_j^e(s) \right\} - i \frac{f_j^p(s)}{a_0} \right] ds, \quad j = 1, 2. \quad (2)$$

In the above, f_j^e and f_j^p are attenuation functions for evanescent and propagating waves, respectively, in each j direction ($j = 1, 2$). $a_0 (= kb)$ denotes dimensionless frequency, k is a wave number, and b is a characteristic length of the system. Referring to the domain configuration of Fig. 2, the attenuation functions $f_j^{e,p} (j = 1, 2)$ are defined as

$$f_j^{e,p}(\mathbf{x}) = \begin{cases} 0, & |x_j| < |x_j^{\text{itf}}|, \\ \frac{3b}{2L_j^{\text{PML}}} \log\left(\frac{1}{|R|}\right) \left(\frac{x_j - x_j^{\text{itf}}}{L_j^{\text{PML}}}\right)^2, & |x_j| \geq |x_j^{\text{itf}}|, \end{cases} \quad (3)$$

where x_j^{itf} is the regular domain–PML interface coordinate in the x_j direction, and L_j^{PML} is the length of the PML in the x_j direction, as shown in Fig. 2. R is a complex-valued user-tunable reflection coefficient controlling the amount of reflection from the fixed exterior PML boundaries (see [11] for details). Eq. (3) implies that $f_j^{e,p}(\mathbf{x})$ are quadratic functions within the PMLs, but vanish in the regular

domain. Thus, the coordinate $\tilde{x}_j \equiv x_j$ within the regular domain, is continuous across the interface between the regular and PML domains (at $x_j = x_j^{\text{itf}}$), and is “stretched” within the PML. Then, the forward problem becomes (see [11] for the derivation):

Find $u(\mathbf{x}, t)$ and $\mathbf{s}(\mathbf{x}, t)$, such that:

$$f_m \frac{\partial^2 v}{\partial t^2} + c_s g_c \frac{\partial v}{\partial t} + c_s^2 g_k v - \nabla \cdot \left(\tilde{\mathbf{F}}^e \frac{\partial \mathbf{s}}{\partial t} + \tilde{\mathbf{F}}^p \mathbf{s} \right) = 0, \quad \text{in } \Omega, \quad t \in (0, T], \quad (4a)$$

$$\mathbf{F}^e \frac{\partial^2 \mathbf{s}}{\partial t^2} + \mathbf{F}^p \frac{\partial \mathbf{s}}{\partial t} - c_s^2 \nabla \left(\frac{\partial v}{\partial t} \right) = 0, \quad \text{in } \Omega, \quad t \in (0, T], \quad (4b)$$

$$v(\mathbf{x}, t) = 0, \quad \text{on } \Gamma_{\text{fixed}}, \quad t \in (0, T], \quad (5a)$$

$$\frac{\partial s_2}{\partial t}(\mathbf{x}, t) = p(\mathbf{x}, t), \quad \text{on } \Gamma_{\text{free}}, \quad t \in (0, T], \quad (5b)$$

$$v(\mathbf{x}, 0) = 0, \quad \frac{\partial v}{\partial t}(\mathbf{x}, 0) = 0, \quad \mathbf{s}(\mathbf{x}, 0) = 0, \quad \frac{\partial \mathbf{s}}{\partial t}(\mathbf{x}, 0) = 0, \quad \text{in } \Omega, \quad (5c)$$

where \mathbf{x} denotes location, and t denotes time. In the above, $u(\mathbf{x}, t)$ is a normalized (scalar) displacement with respect to the soil's density ρ , i.e., $u(\mathbf{x}, t) = \rho u(\mathbf{x}, t)$, in which $u(\mathbf{x}, t)$ is the physical displacement. Throughout we assume that the material density is constant (a reasonable assumption in geotechnical site investigations). $\mathbf{s}(\mathbf{x}, t)$ denotes stress memories or histories defined as

$$\mathbf{s}(\mathbf{x}, t) = \int_0^t \boldsymbol{\sigma}(\mathbf{x}, \tau) d\tau, \quad \mathbf{s} = [s_1 \ s_2]^T, \quad (6)$$

such that:

$$\frac{\partial \mathbf{s}}{\partial t}(\mathbf{x}, t) = \boldsymbol{\sigma}(\mathbf{x}, t), \quad (7a)$$

$$\frac{\partial^2 \mathbf{s}}{\partial t^2}(\mathbf{x}, t) = \frac{\partial \boldsymbol{\sigma}}{\partial t}(\mathbf{x}, t), \quad (7b)$$

in which $\boldsymbol{\sigma} = [\sigma_{31} \ \sigma_{32}]^T$ is a vector of shear stress components; $c_s (= \sqrt{\mu/\rho})$ denotes shear wave velocity; f_m , g_c , and g_k denote PML attenuation functions defined in terms of f_j^e and g_j^p ($j = 1, 2$) as

$$f_m = (1 + f_1^e)(1 + f_2^e), \quad (8a)$$

$$g_c = g_2^p(1 + f_1^e) + g_1^p(1 + f_2^e), \quad (8b)$$

$$g_k = g_1^p g_2^p, \quad (8c)$$

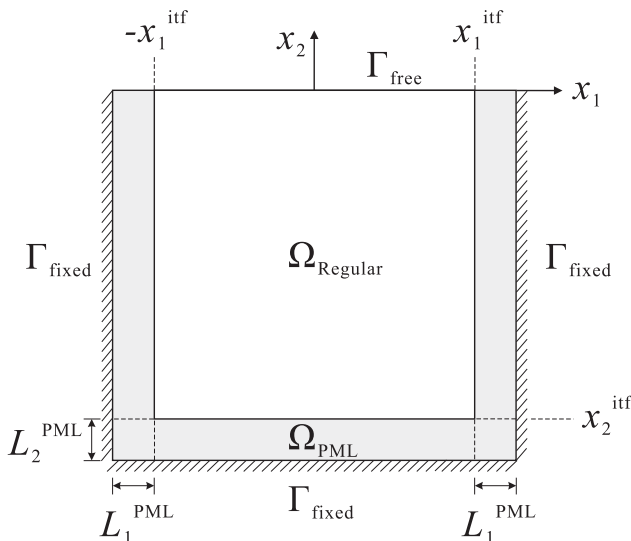


Fig. 2. Schematic of the combined regular-PML-domain in two-dimensions.

where $g_j^p = f_j^p/b$ are normalized attenuation functions with respect to b [11]. \mathbf{F}^e , \mathbf{F}^p , \mathbf{F}^e , and \mathbf{F}^p are stretch tensors defined as [9–11]:

$$\tilde{\mathbf{F}}^e = \begin{bmatrix} 1 + f_2^e & 0 \\ 0 & 1 + f_1^e \end{bmatrix}, \quad \tilde{\mathbf{F}}^p = \begin{bmatrix} c_s g_2^p & 0 \\ 0 & c_s g_1^p \end{bmatrix}, \quad (9)$$

$$\mathbf{F}^e = \begin{bmatrix} 1 + f_1^e & 0 \\ 0 & 1 + f_2^e \end{bmatrix}, \quad \mathbf{F}^p = \begin{bmatrix} c_s g_1^p & 0 \\ 0 & c_s g_2^p \end{bmatrix}. \quad (10)$$

Eq. (4) are the mixed displacement-stress memory ($v - \mathbf{s}$) equations of motion governing the propagation of SH waves in the PML-truncated domain. Within the regular domain ($f_j^e = 0, g_j^p = 0, j = 1, 2$), and upon elimination of the stress, the equations reduce to the two-dimensional wave Eq. (1). Notice that the mixed PML equations maintain the second-order temporal character of the original wave equation. Condition (5a) implies that the PML is fixed on the side and bottom edges ($\mathbf{x} \in \Gamma_{\text{fixed}}$), whereas condition (5b) represents the source excitation $p(t)$ applied on the free surface ($\mathbf{x} \in \Gamma_{\text{free}}$). The system is initially at rest by virtue of conditions (5c).

3. Inverse modeling using PDE-constrained optimization

We discuss next the inverse PML formulation aimed at reconstructing the material profile within the PML-truncated domain. The goal is to recover the heterogeneous shear wave velocity profile (c_s) of Ω_{Regular} .

3.1. The least-squares misfit problem

Referring to Fig. 1(b), the inverse problem for reconstructing the shear wave velocity profile (c_s) in the PML-truncated domain can be cast as follows:

$$\text{Minimize : } \mathcal{J} = \mathcal{F}_m + \mathcal{R}_{c_s}(c_s) \\ = \frac{1}{2} \int_0^T \int_{\Gamma_m} [v(\mathbf{x}, t) - v_m(\mathbf{x}, t)]^2 d\Gamma_m dt + \mathcal{R}_{c_s}(c_s) \quad (11)$$

subject to (4) and (5).

In (11), \mathcal{F}_m is the response misfit defined in the least-squares sense, Γ_m denotes the part of the surface occupied by measuring stations (sensor locations), and $v_m(\mathbf{x}, t)$ is the measured displacement response on Γ_m . In addition to the response misfit \mathcal{F}_m , the objective functional \mathcal{J} comprises a regularization term \mathcal{R}_{c_s} introduced to alleviate solution multiplicity. Candidate regularization schemes are discussed below.

3.2. Tikhonov (TN) regularization

Tikhonov-type regularization is defined as the L^2 -norm of the gradient of material parameters [30]. Let $\mathcal{R}_{c_s}^{\text{TN}}$ denote the Tikhonov regularization term associated with the material parameter (inversion variable) c_s , then:

$$\mathcal{R}_{c_s}^{\text{TN}}(c_s) = \frac{R_{c_s}}{2} \int_{\Omega} \nabla c_s \cdot \nabla c_s d\Omega, \quad (12)$$

where R_{c_s} is a scalar, user-defined, regularization factor. The TN scheme typically enforces smooth spatial variation of the material parameter, penalizing its gradient. Therefore, the TN scheme reconstructs well smooth target profiles, but tends to smoothen discontinuities of sharply-varying target profiles.

3.3. Total variation (TV) regularization

The total variation regularization $\mathcal{R}_{c_s}^{\text{TV}}$ is defined as [31]:

$$\mathcal{R}_{c_s}^{\text{TV}}(c_s) = R_{c_s} \int_{\Omega} (\nabla c_s \cdot \nabla c_s + \epsilon)^{\frac{1}{2}} d\Omega, \quad (13)$$

where R_{c_s} is, again, a regularization factor. $\mathcal{R}_{c_s}^{\text{TV}}$ is a bounded variation semi-norm, modified by the small parameter ϵ . The addition of ϵ makes $\mathcal{R}_{c_s}^{\text{TV}}$ differentiable when $\nabla c_s = 0$. The TV scheme typically permits discontinuities of the material parameter. At the same time, it penalizes spurious material oscillations in otherwise smooth regions. Therefore, the TV scheme performs better when reconstructing sharply-varying profiles than the TN scheme.

3.4. Lagrangian functional

We recast the inverse problem as an unconstrained optimization problem by defining a Lagrangian functional \mathcal{L} as

$$\mathcal{L}(v, s_1, s_2, \lambda_v, \lambda_{s_1}, \lambda_{s_2}, \lambda_B, c_s) \\ = \frac{1}{2} \int_0^T \int_{\Gamma_m} [v(\mathbf{x}, t) - v_m(\mathbf{x}, t)]^2 d\Gamma_m dt + \mathcal{R}_{c_s}(c_s) \\ + \int_{\Omega} \int_0^T \lambda_v \left[f_m \frac{\partial^2 v}{\partial t^2} + c_s g_c \frac{\partial v}{\partial t} + c_s^2 g_k v - \nabla \cdot \left(\tilde{\mathbf{F}}^e \frac{\partial \mathbf{s}}{\partial t} + \tilde{\mathbf{F}}^p \mathbf{s} \right) \right] dtd\Omega \\ + \int_{\Omega} \int_0^T \lambda_{s_1} \left[(1 + f_1^e) \frac{\partial^2 s_1}{\partial t^2} + c_s g_1^p \frac{\partial s_1}{\partial t} - c_s^2 \frac{\partial^2 v}{\partial x_1 \partial t} \right] dtd\Omega \\ + \int_{\Omega} \int_0^T \lambda_{s_2} \left[(1 + f_2^e) \frac{\partial^2 s_2}{\partial t^2} + c_s g_2^p \frac{\partial s_2}{\partial t} - c_s^2 \frac{\partial^2 v}{\partial x_2 \partial t} \right] dtd\Omega \\ + \int_{\Gamma_{\text{free}}} \int_0^T \lambda_B \left(\frac{\partial s_2}{\partial t} - p \right) dtd\Gamma_{\text{free}}. \quad (14)$$

In (14), the objective functional \mathcal{J} is augmented via the weak imposition of the governing PDEs and the boundary condition (5b) using Lagrange multipliers λ_v , λ_{s_1} , λ_{s_2} , and λ_B . In short, (14) can be written as

$$\mathcal{L} = \mathcal{F}_m + \mathcal{R}_{c_s} + \mathcal{F}_s, \quad (15)$$

where \mathcal{F}_s is the side-imposed functional with the Lagrange multipliers. The boundary condition (5a), and the initial conditions (5c) will be explicitly imposed in the semi-discrete forms. We then seek to satisfy the stationarity of \mathcal{L} , by requiring that the first variations of \mathcal{L} vanish. There result the following first-order optimality conditions:

3.4.1. The first optimality condition

We enforce the vanishing of the variation of \mathcal{L} with respect to the Lagrange multipliers ($\lambda_v, \lambda_{s_1}, \lambda_{s_2}, \lambda_B$), i.e.,

$$\delta_{\lambda_v} \mathcal{L} = 0, \quad (16a)$$

$$\delta_{\lambda_{s_1}} \mathcal{L} = 0, \quad (16b)$$

$$\delta_{\lambda_{s_2}} \mathcal{L} = 0, \quad (16c)$$

$$\delta_{\lambda_B} \mathcal{L} = 0. \quad (16d)$$

Eq. (16) result in the *state* (or *forward*) problem, which is identical to the problem described by (4) and (5).

3.4.2. The second optimality condition

Similarly, we require the vanishing of the variation of \mathcal{L} with respect to the state variables v, s_1 , and s_2 , i.e.,

$$\delta_v \mathcal{L} = 0, \quad (17a)$$

$$\delta_{s_1} \mathcal{L} = 0, \quad (17b)$$

$$\delta_{s_2} \mathcal{L} = 0. \quad (17c)$$

Eq. (17a) results in:

$$\begin{aligned} & \int_0^T \int_{\Gamma_m} [v(\mathbf{x}, t) - v_m(\mathbf{x}, t)] \delta v(\mathbf{x}, t) d\Gamma_m dt \\ & + \int_{\Omega} \int_0^T \lambda_v \left[f_m \frac{\partial^2 \delta v}{\partial t^2} + c_s g_c \frac{\partial \delta v}{\partial t} + c_s^2 g_k \delta v \right] dt d\Omega \\ & + \int_{\Omega} \int_0^T -\lambda_{s_1} c_s^2 \frac{\partial^2 \delta v}{\partial x_1 \partial t} dt d\Omega + \int_{\Omega} \int_0^T -\lambda_{s_2} c_s^2 \frac{\partial^2 \delta v}{\partial x_2 \partial t} dt d\Omega = 0. \end{aligned} \quad (18)$$

Eq. (17b) results in:

$$\begin{aligned} & \int_{\Omega} \int_0^T - \left[\lambda_v (1 + f_2^e) \frac{\partial^2 \delta s_1}{\partial x_1 \partial t} + \lambda_v g_2^p \frac{\partial}{\partial x_1} (c_s \delta s_1) \right] dt d\Omega \\ & + \int_{\Omega} \int_0^T \lambda_{s_1} \left[(1 + f_1^e) \frac{\partial^2 \delta s_1}{\partial t^2} + c_s g_1^p \frac{\partial \delta s_1}{\partial t} \right] dt d\Omega = 0. \end{aligned} \quad (19)$$

Eq. (17c) results in:

$$\begin{aligned} & \int_{\Omega} \int_0^T - \left[\lambda_v (1 + f_1^e) \frac{\partial^2 \delta s_2}{\partial x_2 \partial t} + \lambda_v g_1^p \frac{\partial}{\partial x_2} (c_s \delta s_2) \right] dt d\Omega \\ & + \int_{\Omega} \int_0^T \lambda_{s_2} \left[(1 + f_2^e) \frac{\partial^2 \delta s_2}{\partial t^2} + c_s g_2^p \frac{\partial \delta s_2}{\partial t} \right] dt d\Omega \\ & + \int_{\Gamma_{\text{free}}} \int_0^T \lambda_B \frac{\partial \delta s_2}{\partial t} dt d\Gamma = 0. \end{aligned} \quad (20)$$

Using integration by parts in both space and time for Eqs. (18)–(20), and taking into account that δv , δs_1 , and δs_2 are arbitrary, we obtain the following adjoint problem:

Find $\lambda_v(\mathbf{x}, t)$, $\lambda_{s_1}(\mathbf{x}, t)$, and $\lambda_{s_2}(\mathbf{x}, t)$, such that:

$$f_m \frac{\partial^2 \lambda_v}{\partial t^2} - c_s g_c \frac{\partial \lambda_v}{\partial t} + c_s^2 g_k \lambda_v - \nabla \cdot \left(c_s^2 \frac{\partial \lambda_s}{\partial t} \right) = 0, \quad \text{in } \Omega, \quad t \in [0, T], \quad (21a)$$

$$\mathbf{F}^e \frac{\partial^2 \lambda_s}{\partial t^2} - \mathbf{F}^p \frac{\partial \lambda_s}{\partial t} + \tilde{\mathbf{F}}^p \nabla \lambda_v - \tilde{\mathbf{F}}^e \nabla \left(\frac{\partial \lambda_v}{\partial t} \right) = 0, \quad \text{in } \Omega, \quad t \in [0, T], \quad (21b)$$

and subject to

$$\lambda_v(\mathbf{x}, t) = 0, \quad \text{on } \Gamma_{\text{fixed}}, \quad t \in [0, T], \quad (22a)$$

$$c_s^2 \frac{\partial \lambda_{s_2}}{\partial t}(\mathbf{x}, t) = -[v(\mathbf{x}, t) - v_m(\mathbf{x}, t)], \quad \text{on } \Gamma_m, \quad t \in [0, T], \quad (22b)$$

$$c_s^2 \frac{\partial \lambda_{s_2}}{\partial t}(\mathbf{x}, t) = 0, \quad \text{on } \Gamma_{\text{free}} \setminus \Gamma_m, \quad t \in [0, T], \quad (22c)$$

$$\lambda_v(\mathbf{x}, t) = 0, \quad \frac{\partial \lambda_v}{\partial t}(\mathbf{x}, T) = 0, \quad \lambda_s(\mathbf{x}, T) = 0, \quad \frac{\partial \lambda_s}{\partial t}(\mathbf{x}, T) = 0, \quad \text{in } \Omega, \quad (22d)$$

where $\lambda_s = [\lambda_{s_1}, \lambda_{s_2}]^T$. Notice that the adjoint problem is driven by the misfit between the computed and observed responses, as per (22b). Thus, once the state solution $v(\mathbf{x}, t)$ is obtained, the solution of the adjoint problem yields λ_v and λ_s . Notice also that the adjoint problem is a final-value problem as opposed to the initial-value state problem. The adjoint equations are also PML-endowed and mixed, with λ_v and λ_s playing roles analogous to v and \mathbf{s} of the state problem.

3.4.3. The third optimality condition

Lastly, we impose the vanishing of the variation of \mathcal{L} with respect to the material parameter c_s , i.e.,

$$\delta_{c_s} \mathcal{L} = 0, \quad (23)$$

which results in the following equation:

$$\begin{aligned} & R_{c_s} \int_{\Omega} \nabla \delta c_s \cdot \nabla c_s d\Omega \\ & + \int_{\Omega} \int_0^T \lambda_v \left[\delta c_s g_c \frac{\partial v}{\partial t} + 2c_s \delta c_s g_k v - g_2^p \frac{\partial}{\partial x_1} (\delta c_s s_1) - g_1^p \frac{\partial}{\partial x_2} (\delta c_s s_2) \right] dt d\Omega \\ & + \int_{\Omega} \int_0^T \lambda_{s_1} \left[\delta c_s g_1^p \frac{\partial s_1}{\partial t} - 2c_s \delta c_s \frac{\partial^2 v}{\partial x_1 \partial t} \right] dt d\Omega \\ & + \int_{\Omega} \int_0^T \lambda_{s_2} \left[\delta c_s g_2^p \frac{\partial s_2}{\partial t} - 2c_s \delta c_s \frac{\partial^2 v}{\partial x_2 \partial t} \right] dt d\Omega = 0. \end{aligned} \quad (24)$$

In (24), TN regularization has been assumed. By using integration by parts in (24), and taking into account the boundary conditions of the state and adjoint problems, as well as the fact that δc_s is arbitrary, we obtain the following boundary-value control problem:

Find $c_s(\mathbf{x})$ such that:

$$\begin{aligned} & -R_{c_s} \Delta c_s \\ & + \int_0^T \left\{ \lambda_v g_c \frac{\partial v}{\partial t} + 2\lambda_v c_s g_k v + \nabla \lambda_v \cdot \left[\frac{1}{c_s} (\tilde{\mathbf{F}}^p \mathbf{s}) \right] \right. \\ & \left. + \lambda_s \cdot \left[\frac{1}{c_s} (\mathbf{F}^p \frac{\partial \mathbf{s}}{\partial t}) \right] - 2c_s \lambda_s \cdot \nabla \left(\frac{\partial v}{\partial t} \right) \right\} dt = 0, \quad \text{in } \Omega, \end{aligned} \quad (25)$$

subject to

$$\frac{\partial c_s}{\partial n} = 0, \quad \text{on } \Gamma_{\text{free}} \cup \Gamma_{\text{fixed}}, \quad (26)$$

where (26) is a Neumann-type boundary condition for c_s . In (25), the PML attenuation functions g_c , g_k , and the stretch tensors $\tilde{\mathbf{F}}^p$, \mathbf{F}^p vanish within the regular domain, since $f_j^{e,p}$ become zero in the regular domain, per (3). Therefore, the control Eq. (25) is simplified within the regular domain as

$$-R_{c_s} \Delta c_s + \int_0^T \left[-2c_s \lambda_s \cdot \nabla \left(\frac{\partial v}{\partial t} \right) \right] dt = 0, \quad \text{in } \Omega_{\text{Regular}}. \quad (27)$$

We use integration by parts in time for the second term of the left-hand-side of (27), to obtain:

$$\begin{aligned} & \int_0^T \left[-2c_s \lambda_s \cdot \nabla \left(\frac{\partial v}{\partial t} \right) \right] dt = -2c_s \left(\lambda_s \cdot \nabla v|_0^T - \int_0^T \frac{\partial \lambda_s}{\partial t} \cdot \nabla v dt \right) \\ & = 2c_s \int_0^T \frac{\partial \lambda_s}{\partial t} \cdot \left(\frac{1}{c_s^2} \frac{\partial \mathbf{s}}{\partial t} \right) dt \\ & = \frac{2}{c_s} \int_0^T \frac{\partial \lambda_s}{\partial t} \cdot \frac{\partial \mathbf{s}}{\partial t} dt, \end{aligned} \quad (28)$$

where (4b) was used to provide $\nabla v = \frac{1}{c_s^2} \frac{\partial \mathbf{s}}{\partial t}$ (note that $\mathbf{F}^e = \mathbf{I}$ and $\mathbf{F}^p = \mathbf{0}$ in the regular domain), while the initial conditions (5c) and the final condition $\lambda_s(\mathbf{x}, T) = 0$ (22d) were utilized as well. Then, (27) can be rewritten in the regular domain as

$$-R_{c_s} \Delta c_s + \frac{2}{c_s} \int_0^T \frac{\partial \lambda_s}{\partial t} \cdot \frac{\partial \mathbf{s}}{\partial t} dt = 0, \quad \text{in } \Omega_{\text{Regular}}. \quad (29)$$

If the TV regularization scheme were used instead, the first term of (29) would be modified, and the resulting control equation would read:

$$\begin{aligned} & -R_{c_s} (\nabla c_s \cdot \nabla c_s + \epsilon)^{-\frac{3}{2}} [(\nabla c_s \cdot \nabla c_s + \epsilon) \Delta c_s - \nabla c_s \cdot (\mathbf{H} \nabla c_s)] \\ & + \frac{2}{c_s} \int_0^T \frac{\partial \lambda_s}{\partial t} \cdot \frac{\partial \mathbf{s}}{\partial t} dt = 0, \quad \text{in } \Omega_{\text{Regular}}, \end{aligned} \quad (30)$$

in which \mathbf{H} is the Hessian of c_s . We remark that the TV scheme leads to a nonlinear operator in the control equation, as opposed to the Laplacian operator that results when the TN regularization is used.

4. The inversion process

Upon discretization, the derived state, adjoint, and control problems lead to a classic KKT system. We have two possible ways for solving the KKT system. One approach is to solve the system for all of the state (v, s_1, s_2) , adjoint $(\lambda_v, \lambda_{s_1}, \lambda_{s_2}, \lambda_B)$, and control (c_s) variables using a full-space method, i.e., solving for all variables simultaneously. However, the associated computational cost is substantial. Alternatively, we could use a reduced-space method, where we seek solutions in the space of the material property c_s . First, we solve the state problem (4) and (5) for the state variables v, s_1 , and s_2 assuming a distribution of the material property c_s . By doing so, the first optimality condition is satisfied. Then, we solve the adjoint problem (21) and (22) to obtain the adjoint variables λ_v, λ_{s_1} , and λ_{s_2} based on the state solutions computed in the first step. By doing so, we satisfy the second optimality condition. As a last step, the material property c_s is updated in order for the control equation to be satisfied. Notice that the left-hand-side of (29) (or (30)) now implies the continuous form of the reduced gradient $(\nabla_{c_s} \mathcal{L})$. We use a conjugate gradient method with inexact line search to iteratively update the material property using the most recent state and adjoint solutions.

4.1. Semi-discrete form of the state problem

In order to solve the state problem, we employ a mixed finite-element procedure, where the displacement v and the two stress memories s_1 and s_2 are treated as independent variables that need to be approximated separately [32–34]. We seek $v \simeq v_h \in H^h \subset H_0^1(\Omega)$ and s_1 (or s_2) $\simeq (s_1)_h$ (or $(s_2)_h$) $\in Q^h \subset L^2(\Omega)$ such that (4) be satisfied [11]. Thus the trial functions $v(\mathbf{x}, t)$, $s_1(\mathbf{x}, t)$, and $s_2(\mathbf{x}, t)$ are discretized as (the test functions are similarly discretized using the same interpolants):

$$v(\mathbf{x}, t) \simeq \phi(\mathbf{x})^T \mathbf{v}(t), \quad (31a)$$

$$s_1(\mathbf{x}, t) \simeq \psi(\mathbf{x})^T \mathbf{s}_1(t), \quad (31b)$$

$$s_2(\mathbf{x}, t) \simeq \psi(\mathbf{x})^T \mathbf{s}_2(t). \quad (31c)$$

In (31), ϕ and ψ are vectors of approximants associated with nodal displacements ($\mathbf{v} (= \rho \mathbf{u})$) and stress memories (\mathbf{s}_1 and \mathbf{s}_2), respectively. We opted for a quadratic approximant pair for both ϕ and ψ , which numerically has been seen to yield stable solutions (a linear approximant pair is also possible).¹ Introducing the approximants to the weak forms results in the following semi-discrete form [11]:

$$\begin{bmatrix} \mathbf{M}_{11}^{st} & \mathbf{0} & \mathbf{0} \\ \mathbf{0} & \mathbf{M}_{22}^{st} & \mathbf{0} \\ \mathbf{0} & \mathbf{0} & \mathbf{M}_{33}^{st} \end{bmatrix} \begin{bmatrix} \dot{\mathbf{v}} \\ \dot{\mathbf{s}}_1 \\ \dot{\mathbf{s}}_2 \end{bmatrix} + \begin{bmatrix} \mathbf{C}_{11}^{st} & \mathbf{C}_{12}^{st} & \mathbf{C}_{13}^{st} \\ \mathbf{C}_{21}^{st} & \mathbf{C}_{22}^{st} & \mathbf{0} \\ \mathbf{C}_{31}^{st} & \mathbf{0} & \mathbf{C}_{33}^{st} \end{bmatrix} \begin{bmatrix} \mathbf{v} \\ \mathbf{s}_1 \\ \mathbf{s}_2 \end{bmatrix} + \begin{bmatrix} \mathbf{K}_{11}^{st} & \mathbf{K}_{12}^{st} & \mathbf{K}_{13}^{st} \\ \mathbf{0} & \mathbf{0} & \mathbf{0} \\ \mathbf{0} & \mathbf{0} & \mathbf{0} \end{bmatrix} \begin{bmatrix} \mathbf{v} \\ \mathbf{s}_1 \\ \mathbf{s}_2 \end{bmatrix} = \begin{bmatrix} \int_{\Gamma} \phi \left(\tilde{\mathbf{F}}^e \frac{\partial \mathbf{s}}{\partial t} + \tilde{\mathbf{F}}^p \mathbf{s} \right) \cdot \mathbf{n} d\Gamma \\ \mathbf{0} \\ \mathbf{0} \end{bmatrix}, \quad (32)$$

¹ Both the state and adjoint problems are mixed, and as such the pair of approximants should be chosen such that the Ladyshenskaja–Babuška–Brezzi (LBB) condition be satisfied; we have not performed a formal analysis of the LBB condition, but numerically, both linear and quadratic pairs have yielded stable results.

where

$$\mathbf{M}_{11}^{st} = \int_{\Omega} f_m \phi \phi^T d\Omega, \quad (33a)$$

$$\mathbf{M}_{22}^{st} = \int_{\Omega} (1 + f_1^e) \psi \psi^T d\Omega, \quad (33b)$$

$$\mathbf{M}_{33}^{st} = \int_{\Omega} (1 + f_2^e) \psi \psi^T d\Omega, \quad (33c)$$

$$\mathbf{C}_{11}^{st} = \int_{\Omega} c_s g_c \phi \phi^T d\Omega, \quad (34a)$$

$$\mathbf{C}_{12}^{st} = \int_{\Omega} (1 + f_2^e) \frac{\partial \phi}{\partial x_1} \psi^T d\Omega, \quad (34b)$$

$$\mathbf{C}_{13}^{st} = \int_{\Omega} (1 + f_1^e) \frac{\partial \phi}{\partial x_2} \psi^T d\Omega, \quad (34c)$$

$$\mathbf{C}_{21}^{st} = \int_{\Omega} -c_s^2 \psi \frac{\partial \phi^T}{\partial x_1} d\Omega, \quad (34d)$$

$$\mathbf{C}_{22}^{st} = \int_{\Omega} c_s g_1^p \psi \psi^T d\Omega, \quad (34e)$$

$$\mathbf{C}_{31}^{st} = \int_{\Omega} -c_s^2 \psi \frac{\partial \phi^T}{\partial x_2} d\Omega, \quad (34f)$$

$$\mathbf{C}_{33}^{st} = \int_{\Omega} c_s g_2^p \psi \psi^T d\Omega, \quad (34g)$$

$$\mathbf{K}_{11}^{st} = \int_{\Omega} c_s^2 g_k \phi \phi^T d\Omega, \quad (35a)$$

$$\mathbf{K}_{12}^{st} = \int_{\Omega} c_s g_2^p \frac{\partial \phi}{\partial x_1} \psi^T d\Omega, \quad (35b)$$

$$\mathbf{K}_{13}^{st} = \int_{\Omega} c_s g_1^p \frac{\partial \phi}{\partial x_2} \psi^T d\Omega. \quad (35c)$$

In (32), \mathbf{M}^{st} , \mathbf{C}^{st} , and \mathbf{K}^{st} denote the mass-like, damping-like, and stiffness-like matrices of the semi-discrete form of the state problem, where subscripts denote the sub-matrix index, and the superscript 'st' implies the state problem. $[\mathbf{v} \ \mathbf{s}_1 \ \mathbf{s}_2]^T$ is a vector of nodal unknowns comprising the nodal displacement \mathbf{v} and the two nodal stress memories \mathbf{s}_1 and \mathbf{s}_2 , and a dot over a vector of nodal quantities denotes differentiation with respect to time of the subtended vector.

4.2. Semi-discrete form of the adjoint problem

To solve the adjoint problem, we use again the mixed finite-element procedure, where λ_v, λ_{s_1} , and λ_{s_2} are treated as independent variables and approximated separately. We seek $\lambda_v \simeq (\lambda_v)_h \in H^h \subset H_0^1(\Omega)$ and λ_{s_1} (or λ_{s_2}) $\simeq (\lambda_{s_1})_h$ (or $(\lambda_{s_2})_h$) $\in Q^h \subset L^2(\Omega)$ such that (21) be satisfied. Equations (21) are multiplied by test functions $w(\mathbf{x})$, $p(\mathbf{x})$, and $q(\mathbf{x})$, respectively, and then integrated over the entire domain $\Omega_{\text{Regular}} \cup \Omega_{\text{PML}}$ to arrive at the corresponding weak forms:

$$\int_{\Omega} w \left(f_m \frac{\partial^2 \lambda_v}{\partial t^2} - c_s g_c \frac{\partial \lambda_v}{\partial t} + c_s^2 g_k \lambda_v \right) d\Omega + \int_{\Omega} \nabla w \cdot \left(c_s \frac{\partial \lambda_s}{\partial t} \right) d\Omega = \int_{\Gamma} w c_s^2 \frac{\partial \lambda_s}{\partial t} \cdot \mathbf{n} d\Gamma, \quad (36a)$$

$$\int_{\Omega} p \left[(1 + f_1^e) \frac{\partial^2 \lambda_{s_1}}{\partial t^2} - c_s g_1^p \frac{\partial \lambda_{s_1}}{\partial t} + c_s g_2^p \frac{\partial \lambda_v}{\partial x_1} - (1 + f_2^e) \frac{\partial^2 \lambda_v}{\partial x_1 \partial t} \right] d\Omega = 0, \quad (36b)$$

$$\int_{\Omega} q \left[(1 + f_2^e) \frac{\partial^2 \lambda_{s_2}}{\partial t^2} - c_s g_2^p \frac{\partial \lambda_{s_2}}{\partial t} + c_s g_1^p \frac{\partial \lambda_v}{\partial x_2} - (1 + f_1^e) \frac{\partial^2 \lambda_v}{\partial x_2 \partial t} \right] d\Omega = 0. \quad (36c)$$

To arrive at (36a), the last term of (21a) was integrated by parts. The trial functions $\lambda_v(\mathbf{x}, t)$, $\lambda_{s_1}(\mathbf{x}, t)$, and $\lambda_{s_2}(\mathbf{x}, t)$ are spatially discretized as

$$\lambda_v(\mathbf{x}, t) \simeq \boldsymbol{\phi}(\mathbf{x})^T \lambda_v(t), \quad (37a)$$

$$\lambda_{s_1}(\mathbf{x}, t) \simeq \boldsymbol{\psi}(\mathbf{x})^T \lambda_{s_1}(t), \quad (37b)$$

$$\lambda_{s_2}(\mathbf{x}, t) \simeq \boldsymbol{\psi}(\mathbf{x})^T \lambda_{s_2}(t). \quad (37c)$$

The three test functions $w(\mathbf{x})$, $p(\mathbf{x})$, and $q(\mathbf{x})$ are similarly discretized as

$$w(\mathbf{x}, t) \simeq \mathbf{W}^T \boldsymbol{\phi}(\mathbf{x}), \quad (38a)$$

$$p(\mathbf{x}, t) \simeq \mathbf{P}^T \boldsymbol{\psi}(\mathbf{x}), \quad (38b)$$

$$q(\mathbf{x}, t) \simeq \mathbf{Q}^T \boldsymbol{\psi}(\mathbf{x}). \quad (38c)$$

Introducing the approximants to the weak forms results in the following semi-discrete form:

$$\begin{bmatrix} \mathbf{M}_{11}^{\text{adj}} & \mathbf{0} & \mathbf{0} \\ \mathbf{0} & \mathbf{M}_{22}^{\text{adj}} & \mathbf{0} \\ \mathbf{0} & \mathbf{0} & \mathbf{M}_{33}^{\text{adj}} \end{bmatrix} \begin{bmatrix} \dot{\lambda}_v \\ \dot{\lambda}_{s_1} \\ \dot{\lambda}_{s_2} \end{bmatrix} + \begin{bmatrix} \mathbf{C}_{11}^{\text{adj}} & \mathbf{C}_{12}^{\text{adj}} & \mathbf{C}_{13}^{\text{adj}} \\ \mathbf{C}_{21}^{\text{adj}} & \mathbf{C}_{22}^{\text{adj}} & \mathbf{0} \\ \mathbf{C}_{31}^{\text{adj}} & \mathbf{0} & \mathbf{C}_{33}^{\text{adj}} \end{bmatrix} \begin{bmatrix} \lambda_v \\ \lambda_{s_1} \\ \lambda_{s_2} \end{bmatrix} + \begin{bmatrix} \mathbf{K}_{11}^{\text{adj}} & \mathbf{0} & \mathbf{0} \\ \mathbf{K}_{21}^{\text{adj}} & \mathbf{0} & \mathbf{0} \\ \mathbf{K}_{31}^{\text{adj}} & \mathbf{0} & \mathbf{0} \end{bmatrix} \begin{bmatrix} \lambda_v \\ \lambda_{s_1} \\ \lambda_{s_2} \end{bmatrix} = \begin{bmatrix} \int_{\Gamma} \boldsymbol{\phi} \boldsymbol{c}_s^2 \frac{\partial \lambda}{\partial t} \cdot \mathbf{n} d\Gamma \\ \mathbf{0} \\ \mathbf{0} \end{bmatrix}, \quad (39)$$

where

$$\mathbf{M}_{11}^{\text{adj}} = \int_{\Omega} f_m \boldsymbol{\phi} \boldsymbol{\phi}^T d\Omega, \quad (40a)$$

$$\mathbf{M}_{22}^{\text{adj}} = \int_{\Omega} (1 + f_1^e) \boldsymbol{\psi} \boldsymbol{\psi}^T d\Omega, \quad (40b)$$

$$\mathbf{M}_{33}^{\text{adj}} = \int_{\Omega} (1 + f_2^e) \boldsymbol{\psi} \boldsymbol{\psi}^T d\Omega, \quad (40c)$$

$$\mathbf{C}_{11}^{\text{adj}} = \int_{\Omega} -c_s g_c \boldsymbol{\phi} \boldsymbol{\phi}^T d\Omega, \quad (41a)$$

$$\mathbf{C}_{12}^{\text{adj}} = \int_{\Omega} c_s^2 \frac{\partial \boldsymbol{\phi}}{\partial x_1} \boldsymbol{\psi}^T d\Omega, \quad (41b)$$

$$\mathbf{C}_{13}^{\text{adj}} = \int_{\Omega} c_s^2 \frac{\partial \boldsymbol{\phi}}{\partial x_2} \boldsymbol{\psi}^T d\Omega, \quad (41c)$$

$$\mathbf{C}_{21}^{\text{adj}} = \int_{\Omega} -(1 + f_2^e) \boldsymbol{\psi} \frac{\partial \boldsymbol{\phi}^T}{\partial x_1} d\Omega, \quad (41d)$$

$$\mathbf{C}_{22}^{\text{adj}} = \int_{\Omega} -c_s g_1^p \boldsymbol{\psi} \boldsymbol{\psi}^T d\Omega, \quad (41e)$$

$$\mathbf{C}_{31}^{\text{adj}} = \int_{\Omega} -(1 + f_1^e) \boldsymbol{\psi} \frac{\partial \boldsymbol{\phi}^T}{\partial x_2} d\Omega, \quad (41f)$$

$$\mathbf{C}_{33}^{\text{adj}} = \int_{\Omega} -c_s g_2^p \boldsymbol{\psi} \boldsymbol{\psi}^T d\Omega, \quad (41g)$$

$$\mathbf{K}_{11}^{\text{adj}} = \int_{\Omega} c_s^2 g_k \boldsymbol{\phi} \boldsymbol{\phi}^T d\Omega, \quad (42a)$$

$$\mathbf{K}_{21}^{\text{adj}} = \int_{\Omega} c_s g_2^p \boldsymbol{\psi} \frac{\partial \boldsymbol{\phi}^T}{\partial x_1} d\Omega, \quad (42b)$$

$$\mathbf{K}_{31}^{\text{adj}} = \int_{\Omega} c_s g_1^p \boldsymbol{\psi} \frac{\partial \boldsymbol{\phi}^T}{\partial x_2} d\Omega. \quad (42c)$$

In (39), \mathbf{M}^{adj} , \mathbf{C}^{adj} , and \mathbf{K}^{adj} represent the mass-like, damping-like, and stiffness-like matrices of the semi-discrete form of the adjoint problem. The superscript ‘adj’ implies the *adjoint problem*. $[\lambda_v \lambda_{s_1} \lambda_{s_2}]^T$ is a vector of nodal unknowns comprising nodal values of the Lagrange multipliers λ_v , λ_{s_1} , and λ_{s_2} . We remark that the sub-matrices of the state and adjoint semi-discrete forms are related to each other via:

$$\mathbf{M}_{ij}^{\text{adj}} = \mathbf{M}_{ij}^{\text{st}}, \quad i = 1, 2, 3, \quad j = 1, 2, 3, \quad (43a)$$

$$\mathbf{C}_{ij}^{\text{adj}} = -(\mathbf{C}_{ji}^{\text{st}})^T, \quad i = 1, 2, 3, \quad j = 1, 2, 3, \quad (43b)$$

$$\mathbf{K}_{ij}^{\text{adj}} = -(\mathbf{K}_{ji}^{\text{st}})^T, \quad i = 1, 2, 3, \quad j = 1, 2, 3. \quad (43c)$$

Eq. (43) suggest that the adjoint problem matrices can be obtained directly from the state problem matrices. The state and adjoint semi-discrete forms can be easily integrated in time using standard integration schemes, even though the damping and stiffness matrices of the state and adjoint semi-discrete forms are non-symmetric.

4.3. State and adjoint time integration

Use of Newmark’s scheme yields the following linear system of equations for the state unknowns \mathbf{u}^{st} at the $(n + 1)$ th time step:

$$\mathbf{K}_{\text{eff}}^{\text{st}} \mathbf{u}_{n+1}^{\text{st}} = [\mathbf{R}_{\text{eff}}^{\text{st}}]_{n+1}, \quad (44)$$

where the effective stiffness matrix $\mathbf{K}_{\text{eff}}^{\text{st}}$, and the effective load vector $[\mathbf{R}_{\text{eff}}^{\text{st}}]_{n+1}$ are given as

$$\mathbf{K}_{\text{eff}}^{\text{st}} = \frac{1}{\beta \Delta t^2} \mathbf{M}^{\text{st}} + \frac{\gamma}{\beta \Delta t} \mathbf{C}^{\text{st}} + \mathbf{K}^{\text{st}}, \quad (45)$$

$$\begin{aligned} [\mathbf{R}_{\text{eff}}^{\text{st}}]_{n+1} &= \mathbf{R}_{n+1}^{\text{st}} + \mathbf{M}^{\text{st}} \left[\frac{1}{\beta \Delta t^2} \mathbf{u}_n^{\text{st}} + \frac{1}{\beta \Delta t} \dot{\mathbf{u}}_n^{\text{st}} + \left(\frac{1}{2\beta} - 1 \right) \ddot{\mathbf{u}}_n^{\text{st}} \right] \\ &+ \mathbf{C}^{\text{st}} \left[\frac{\gamma}{\beta \Delta t} \mathbf{u}_n^{\text{st}} + \left(\frac{\gamma}{\beta} - 1 \right) \dot{\mathbf{u}}_n^{\text{st}} + \Delta t \left(\frac{\gamma}{2\beta} - 1 \right) \ddot{\mathbf{u}}_n^{\text{st}} \right], \end{aligned} \quad (46)$$

where Δt is a time step, and the subscripts n and $n + 1$ denote the n th and $(n + 1)$ th time step, respectively. β and γ are the usual Newmark parameters,² and $\mathbf{R}_{n+1}^{\text{st}}$ is the state nodal load vector at $(n + 1)$ th time step. Once $\mathbf{u}_{n+1}^{\text{st}}$ is obtained by (44), the state velocities $\dot{\mathbf{u}}_{n+1}^{\text{st}}$ and accelerations $\ddot{\mathbf{u}}_{n+1}^{\text{st}}$ can be computed by the following equations:

$$\dot{\mathbf{u}}_{n+1}^{\text{st}} = -\frac{\gamma}{\beta \Delta t} \mathbf{u}_n^{\text{st}} - \left(\frac{\gamma}{\beta} - 1 \right) \dot{\mathbf{u}}_n^{\text{st}} - \frac{\Delta t}{2} \left(\frac{\gamma}{\beta} - 2 \right) \ddot{\mathbf{u}}_n^{\text{st}} + \frac{\gamma}{\beta \Delta t} \mathbf{u}_{n+1}^{\text{st}}, \quad (47)$$

$$\ddot{\mathbf{u}}_{n+1}^{\text{st}} = \frac{1}{\beta \Delta t^2} (\mathbf{u}_{n+1}^{\text{st}} - \mathbf{u}_n^{\text{st}}) - \frac{1}{\beta \Delta t} \dot{\mathbf{u}}_n^{\text{st}} - \left(\frac{1}{2\beta} - 1 \right) \ddot{\mathbf{u}}_n^{\text{st}}. \quad (48)$$

The Newmark method is used to solve the adjoint semi-discrete forms as well. For the final-value adjoint problem, we start from the final conditions (22d) and calculate the adjoint nodal unknowns $\mathbf{u}^{\text{adj}} = [\lambda_v \lambda_{s_1} \lambda_{s_2}]^T$ at successively decreasing times by the following linear system of equations:

$$\mathbf{K}_{\text{eff}}^{\text{adj}} \mathbf{u}_{n-1}^{\text{adj}} = [\mathbf{R}_{\text{eff}}^{\text{adj}}]_{n-1}. \quad (49)$$

In (49), the effective stiffness matrix $\mathbf{K}_{\text{eff}}^{\text{adj}}$ and the effective load vector $[\mathbf{R}_{\text{eff}}^{\text{adj}}]_{n-1}$ are

$$\mathbf{K}_{\text{eff}}^{\text{adj}} = \frac{1}{\beta \Delta t^2} \mathbf{M}^{\text{adj}} - \frac{\gamma}{\beta \Delta t} \mathbf{C}^{\text{adj}} + \mathbf{K}^{\text{adj}}, \quad (50)$$

$$\begin{aligned} [\mathbf{R}_{\text{eff}}^{\text{adj}}]_{n-1} &= \mathbf{R}_{n-1}^{\text{adj}} + \mathbf{M}^{\text{adj}} \left[\frac{1}{\beta \Delta t^2} \mathbf{u}_n^{\text{adj}} - \frac{1}{\beta \Delta t} \dot{\mathbf{u}}_n^{\text{adj}} + \left(\frac{1}{2\beta} - 1 \right) \ddot{\mathbf{u}}_n^{\text{adj}} \right] \\ &+ \mathbf{C}^{\text{adj}} \left[-\frac{\gamma}{\beta \Delta t} \mathbf{u}_n^{\text{adj}} + \left(\frac{\gamma}{\beta} - 1 \right) \dot{\mathbf{u}}_n^{\text{adj}} - \Delta t \left(\frac{\gamma}{2\beta} - 1 \right) \ddot{\mathbf{u}}_n^{\text{adj}} \right]. \end{aligned} \quad (51)$$

Notice that the effective stiffness matrix and the load vector of the adjoint problem $(\mathbf{K}_{\text{eff}}^{\text{adj}}, [\mathbf{R}_{\text{eff}}^{\text{adj}}]_{n-1})$ can be obtained by simply replac-

² In all applications we used $\beta = 0.25(\gamma + 0.5)^2$, and $\gamma = \frac{5}{6}$.

ing Δt by $-\Delta t$ in Eqs. (45), (46) of the state problem. Once $\mathbf{u}_{n-1}^{\text{adj}}$ is obtained by (49), the adjoint velocities $\dot{\mathbf{u}}_{n-1}^{\text{adj}}$ and accelerations $\ddot{\mathbf{u}}_{n-1}^{\text{adj}}$ can be computed by the following equations:

$$\dot{\mathbf{u}}_{n-1}^{\text{adj}} = \frac{\gamma}{\beta \Delta t} \mathbf{u}_n^{\text{adj}} - \left(\frac{\gamma}{\beta} - 1\right) \dot{\mathbf{u}}_n^{\text{adj}} + \frac{\Delta t}{2} \left(\frac{\gamma}{\beta} - 2\right) \ddot{\mathbf{u}}_n^{\text{adj}} - \frac{\gamma}{\beta \Delta t} \mathbf{u}_{n-1}^{\text{adj}}, \quad (52)$$

$$\ddot{\mathbf{u}}_{n-1}^{\text{adj}} = \frac{1}{\beta \Delta t^2} (\mathbf{u}_{n-1}^{\text{adj}} - \mathbf{u}_n^{\text{adj}}) + \frac{1}{\beta \Delta t} \dot{\mathbf{u}}_n^{\text{adj}} - \left(\frac{1}{2\beta} - 1\right) \ddot{\mathbf{u}}_n^{\text{adj}}. \quad (53)$$

4.4. Material parameter updates

By solving the state and adjoint problems as described in Section 4.3, the first and second optimality conditions are automatically satisfied. There remains to update the material property c_s in order to satisfy the third optimality condition. Since we minimize the Lagrangian functional \mathcal{L} in the space of c_s , the left-hand-side of (29)(or (30)) represents the reduced gradient $(\nabla_{c_s} \mathcal{L})$ of the Lagrangian functional. That is, in the case of TN regularization:

$$\nabla_{c_s} \mathcal{L} = -R_{c_s} \Delta c_s + \frac{2}{c_s} \int_0^T \frac{\partial \lambda_s}{\partial t} \cdot \frac{\partial \mathbf{s}}{\partial t} dt, \quad \text{in } \Omega_{\text{Regular}}. \quad (54)$$

If TV regularization is used, the right-hand-side of (54) is replaced by the left-hand-side of (30). The continuous form (54) is evaluated at each nodal point. Since we use quadratic basis functions to interpolate the state and adjoint variables, nodal values of $\frac{\partial \mathbf{s}}{\partial t}$ and $\frac{\partial \lambda_s}{\partial t}$ are directly available from the state and adjoint discrete solutions. At each nodal point the Laplacian (Δc_s) is evaluated using a finite difference scheme. Once the discrete reduced gradient is obtained, we update the nodal values of the material property c_s using a conjugate gradient method with inexact line search. The details follow:

Let us denote by \mathbf{g}_k the discrete reduced gradient at the k -th inversion iteration:

$$\mathbf{g}_k = (\nabla_{c_s} \mathcal{L})_k. \quad (55)$$

We also denote by $(\mathbf{c}_s)_k$ the material property vector comprising nodal values of $c_s(\mathbf{x})$ at the k -th iteration (the number of components in \mathbf{g}_k and $(\mathbf{c}_s)_k$ is the same as the number of nodes, that is, the material parameters are also approximately quadratically); then, $(\mathbf{c}_s)_k$ is updated by

$$(\mathbf{c}_s)_{k+1} = (\mathbf{c}_s)_k + \alpha \mathbf{d}_k, \quad (56)$$

where \mathbf{d}_k is the search direction at $(\mathbf{c}_s)_k$, and α is the step length in the direction of \mathbf{d}_k . The search direction \mathbf{d}_k is determined as

$$\mathbf{d}_k = \begin{cases} -\mathbf{g}_k & (k = 0), \\ -\mathbf{g}_k + \frac{\mathbf{g}_k \cdot \mathbf{g}_{k-1}}{\mathbf{g}_{k-1} \cdot \mathbf{g}_{k-1}} \mathbf{d}_{k-1} & (k \geq 1). \end{cases} \quad (57)$$

We evaluate the misfit functional (11) using the updated material properties $(\mathbf{c}_s)_{k+1}$, and compare it against a preset tolerance. If the tolerance threshold is not met, we set $k \leftarrow k + 1$, and proceed to the next iteration. As is known, the search direction \mathbf{d}_k will be progressively contaminated by errors resulting from the inaccuracies involved in the determination of α , and by the round-off error involved in the accumulation of the $\mathbf{g}_k \cdot \mathbf{g}_k / \mathbf{g}_{k-1} \cdot \mathbf{g}_{k-1}$ terms in (57). Hence, it is necessary that \mathbf{d}_{m+1} be set equal to $-\mathbf{g}_{m+1}$ after every m steps, instead of the usual form (we used $m = 10$) [35].

One can also find an optimal step length α as the local minimizer in the direction of \mathbf{d}_k , but it is, generally, expensive to compute. More practical strategies perform an inexact line search to determine a step length that achieves adequate reduction in the objective functional \mathcal{J} . A popular inexact line search condition requires that α result in sufficient decrease in the objective functional \mathcal{J} , as measured by the following inequality:

Armijo condition or sufficient decrease condition:

$$\mathcal{J}[(\mathbf{c}_s)_k + \alpha \mathbf{d}_k] \leq \mathcal{J}[(\mathbf{c}_s)_k] + \mu \alpha \mathbf{g}_k \cdot \mathbf{d}_k. \quad (58)$$

In practice, μ is chosen to be quite small. ([36]; herein, we used $\mu = 10^{-8}$). In order to choose a step length α satisfying (58), we use the, so-called, *backtracking* approach as summarized in Table 1. In this procedure, the initial step length $\bar{\alpha}$ is usually fixed. If (58) is violated, an acceptable step length α will be found after a finite number of trials by setting $\alpha \leftarrow \rho \alpha$, such that α becomes small enough to satisfy the Armijo condition ($\rho = 0.5$ is a typical value). We summarize the entire inversion process discussed so far in Table 2.

4.5. Regularization factor continuation

Referring to (15) and (24), the reduced gradient (54) can be recast as

$$\nabla_{c_s} \mathcal{L} = R_{c_s} (\nabla_{c_s} \mathcal{F}_r) + (\nabla_{c_s} \mathcal{F}_s), \quad (59)$$

where

$$\nabla_{c_s} \mathcal{F}_r = -\Delta c_s, \quad (60)$$

$$\nabla_{c_s} \mathcal{F}_s = \frac{2}{c_s} \int_0^T \frac{\partial \lambda_s}{\partial t} \cdot \frac{\partial \mathbf{s}}{\partial t} dt. \quad (61)$$

In (59), $\nabla_{c_s} \mathcal{F}_r$ and $\nabla_{c_s} \mathcal{F}_s$ denote the gradients of the regularization and side-imposed functionals, respectively. Eq. (60) results from the TN regularization. If, instead, TV regularization is used, (60) is replaced by

$$\nabla_{c_s} \mathcal{F}_r = -(\nabla_{c_s} \cdot \nabla c_s + \epsilon)^{-\frac{3}{2}} [(\nabla_{c_s} \cdot \nabla c_s + \epsilon) \Delta c_s - \nabla_{c_s} \cdot (\mathbf{H} \nabla c_s)]. \quad (62)$$

$\nabla_{c_s} \mathcal{F}_r$ penalizes high-frequency fluctuations in the recovered profile, such that, the higher R_{c_s} is, the smoother the reconstructed profile becomes. R_{c_s} can have a fixed value throughout the inversion process. However, sharp profiles may not be recoverable if R_{c_s} is too large, and conversely, the inversion process may be more prone to failure due to solution multiplicity if R_{c_s} is too small. Therefore, there is a need to

Table 1
Algorithm 1. Backtracking line search procedure.

Choose $\bar{\alpha} > 0$, ρ , $\mu \in (0, 1)$; set $\alpha \leftarrow \bar{\alpha}$;
repeat
$\alpha \leftarrow \rho \alpha$;
until $\mathcal{J}[(\mathbf{c}_s)_k + \alpha \mathbf{d}_k] \leq \mathcal{J}[(\mathbf{c}_s)_k] + \mu \alpha \mathbf{g}_k \cdot \mathbf{d}_k$
Terminate with $\alpha_k = \alpha$

Table 2
Algorithm 2. Inversion algorithm using a mixed unsplit-field PML scheme; reduced-space approach.

1: Choose $\bar{\alpha}$, ρ , μ , and R_{c_s} ; Set $\alpha = \bar{\alpha}$
2: Set $k = 0$ and convergence tolerance tol
3: Set initial guess of the material property vector $(\mathbf{c}_s)_k$
4: Set $\mathcal{F}_m = tol + 1$
5: while ($\mathcal{F}_m > tol$) do
6: Solve the state problem (4) and (5) to obtain v and $\frac{\partial \mathbf{s}}{\partial t}$
7: Solve the adjoint problem (21) and (22) to obtain $\frac{\partial \lambda_s}{\partial t}$
8: Compute the discrete form of the reduced gradient $\mathbf{g}_k = (\nabla_{c_s} \mathcal{L})_k$ by (54)
9: Compute the search direction \mathbf{d}_k (57)
10: while $[\mathcal{J}[(\mathbf{c}_s)_k + \alpha \mathbf{d}_k] > \mathcal{J}[(\mathbf{c}_s)_k] + \mu \alpha \mathbf{g}_k \cdot \mathbf{d}_k]$ do
11: $\alpha \leftarrow \rho \alpha$
12: end while
13: Update material property vector by $(\mathbf{c}_s)_{k+1} = (\mathbf{c}_s)_k + \alpha \mathbf{d}_k$
14: $k = k + 1$
15: end while

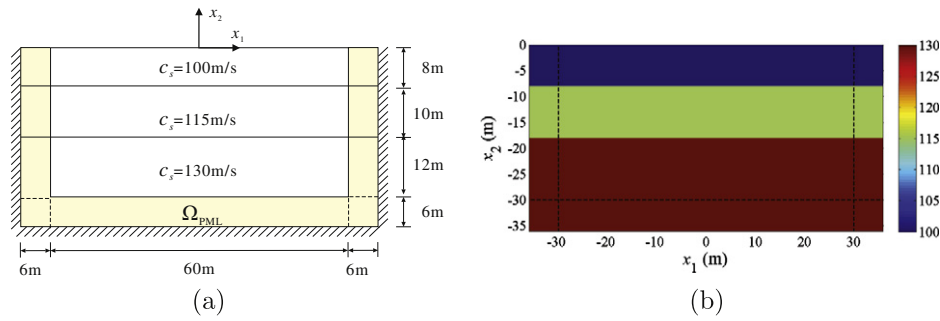


Fig. 3. (a) Configuration of a PML-truncated heterogeneous half-plane with 3 layers; (b) target shear wave velocity profile with 3 layers ($c_s = 100, 115,$ and 130 m/s from top to bottom).

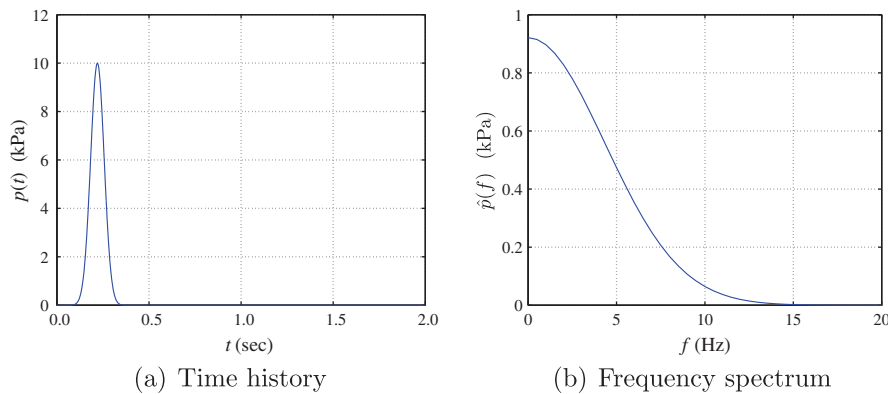


Fig. 4. (a) Source time signal $p(t)$ (Gaussian pulse); (b) frequency spectrum of the Gaussian pulse $p(t)$ with $f_{\max} = 15$ Hz.

continuously modify the regularization factor to avoid such difficulties. Though mindful of various developments for intelligently choosing the regularization factor (e.g. L -curve [37,38]), here we suggest a simple and practical approach to determine the regularization factor at each inversion iteration:

$$\text{Impose } R_{c_s} |\nabla_{c_s} \mathcal{F}_r| < |\nabla_{c_s} \mathcal{F}_s| \Rightarrow R_{c_s} < \frac{|\nabla_{c_s} \mathcal{F}_s|}{|\nabla_{c_s} \mathcal{F}_r|} \quad (63)$$

Thus, R_{c_s} is chosen, at each iteration, to be:

$$R_{c_s} = \mathcal{E} \frac{|\nabla_{c_s} \mathcal{F}_s|}{|\nabla_{c_s} \mathcal{F}_r|}, \quad (64)$$

in which $\mathcal{E} (0 \leq \mathcal{E} \leq 1)$ is a tuning factor controlling the amount of R_{c_s} .

5. Numerical examples

5.1. A model 3-layer problem

We consider first a 60×30 m truncated heterogeneous half-plane, where PMLs (6 m wide) are introduced on the sides and bottom of the truncated domain, as shown in Fig. 3(a). The domain has 3 horizontal layers of shear wave velocities 100, 115, and 130 m/s from surface to bottom. The density is 2000 kg/m^3 for all three layers. Fig. 3(b) depicts the target velocity profile. Notice that the horizontal layers are extended into the PML region, such that the shear wave velocity is constant along lines perpendicular to the regular domain-PML interface, and equal in value to the velocity at the interface.

The domain is discretized using biquadratic elements with element size of 1 m for the regular domain, and 0.5 m for the PML region, respectively. There result 12 elements within each PML

region. A reflection coefficient $|R| = 10^{-8}$ is used for the PML. To illuminate the domain, we apply a Gaussian pulse-type stress load $\sigma_{32} = p(t)$ on the entire surface of the regular domain ($x_2 = 0$), with a maximum frequency of 15 Hz (Fig. 4(a)).³ The time step is 0.0025 s. Sensors that measure the displacement response $u(\mathbf{x}, t)$ are placed at every grid point on the surface of the regular domain (there are 121 surface sensors). We synthesize the sensor readings by solving the forward problem under the target velocity profile, but using a different mesh than that used during the inversion to avoid committing an inverse “crime”. Fig. 5 shows the measured displacement responses at, for example, three sensor locations ($x_1 = 0, 15,$ and 30 m) on the surface; they are used to drive the inversion.

Fig. 6 depicts the reconstructed shear wave velocity profile using both TN and TV regularizations. We started from an initial profile that has a linear variation from 105 to 127 m/s in the vertical direction. Throughout the inversion process, we imposed a fixed regularization factor of $R_{c_s} = 10^{-4}$ for both regularization cases. The fixed (in this case) value of R_{c_s} was computed using (64) as follows: during the first iteration, and due to a homogeneous initial guess, which forces the regularization term to vanish, the value of the regularization factor has no effect ($\nabla_{c_s} \mathcal{F}_r = 0$). At the end of the first iteration, and after the material properties have been updated, we computed the regularization factor using (64) and $\mathcal{E} = 0.05$. As shown in the figure, the TV regularization scheme captures the sharp interfaces better than TN scheme. In Fig. 7, the target, initial guess, and inverted velocity profiles are plotted for the three vertical cross-section lines (lines AA, BB, and CC) of the domain. The TV scheme reconstructs nicely the sharply-varying

³ The expressions for all Gaussian pulses used for the numerical results are given in the Appendix.

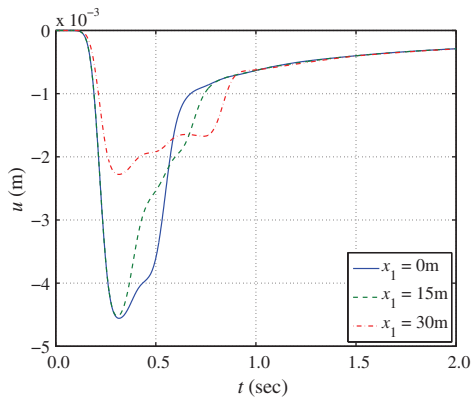
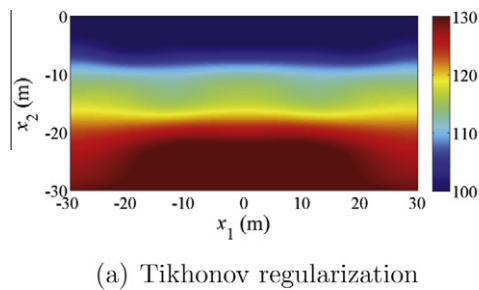


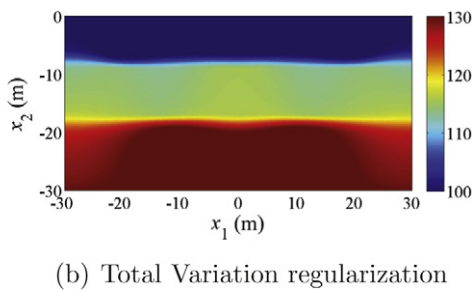
Fig. 5. Measured displacement responses $u(\mathbf{x}, t)$ at 3 surface locations ($x_1 = 0, 15,$ and 30 m). Data are obtained by applying a uniformly-distributed Gaussian pulse with $f_{\max} = 15$ Hz over the entire surface of the 3-layer domain.

target lines, whereas the TN scheme shows a smooth variation, as expected. In Fig. 8, the variation of the misfit (\mathcal{F}_m) is plotted versus the number of inversion iterations for both the TN and TV cases. As seen in the figure, the misfit decreases monotonically as the iteration progresses, with TV showing faster convergence than the TN scheme. Notice that under the TN scheme, the inversion process could not lead to any further reductions of the misfit after approximately 400 iterations. We discuss below how to improve convergence in this case. In Fig. 9, we plot the displacement responses obtained using the converged wave velocity profiles, and compare them against the measured responses at 3 locations on the surface ($x_1 = 0, 15,$ and 30 m). The displayed agreement (in the visual norm) is representative of all surface points, that is, there is very small difference between the computed and measured responses.

In general, the regularization factor R_{c_s} needs to be large at the beginning of the inversion process to assist in narrowing down the feasibility space of the solution. However, as it can be seen in Fig. 6(a), the reconstruction of the layered profile will be somewhat

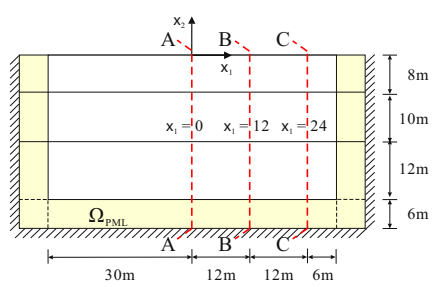


(a) Tikhonov regularization

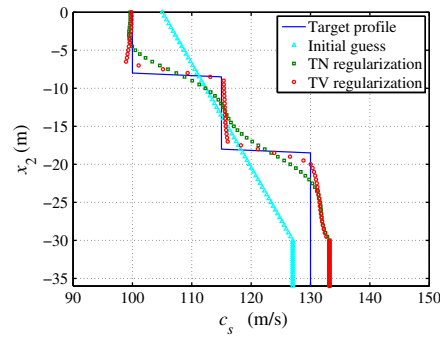


(b) Total Variation regularization

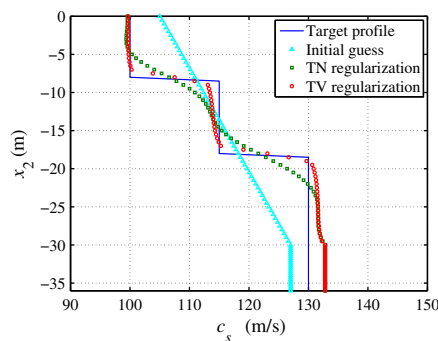
Fig. 6. Inverted shear wave velocity profiles with 3 layers ($R_{c_s} = 10^{-4}$); (a) and (b) were obtained using 440 and 1160 iterations, respectively.



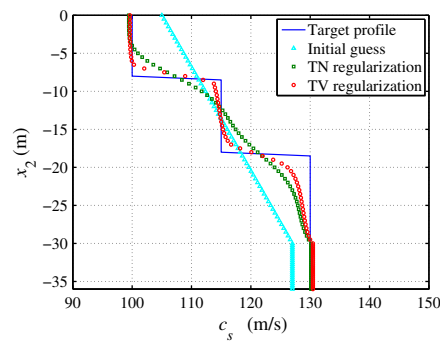
(a) Configuration of the three cross-section lines AA, BB, and CC



(b) Cross section AA



(c) Cross section BB



(d) Cross section CC

Fig. 7. Inverted 3-layer velocity profiles along the three vertical cross-section lines AA, BB, and CC; TN and TV regularization schemes are used with fixed $R_{c_s} = 10^{-4}$.

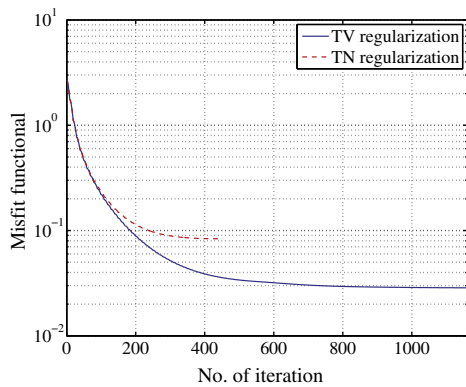


Fig. 8. Misfit \mathcal{F}_m versus number of iterations for the results shown in Fig. 6.

hindered if the regularization factor is large and does not change through the iterations. We use the regularization factor continuation scheme discussed in Section 4.5 to overcome this difficulty. We attempt to recover again the target 3-layer velocity profile using TN regularization, but now assisted by the regularization factor continuation algorithm. Fig. 10 depicts the reconstructed image and the cross-sectional profile (line CC in Fig. 7(a)) using the continuation scheme. We used the same initial guess profile as before (linear profile). The sharp material interfaces are now reconstructed better than when a fixed R_{c_s} is used (Fig. 10(b)). Fig. 11(a) shows that the misfit reduces to less than 1.5% of the initial misfit. By contrast, the misfit reduction for the fixed factor TN regularization is more than 3%, as shown in Fig. 8. Fig. 11(b) shows the variation of the regularization factor as the iterations progress (we used $\varepsilon = 0.9$ as the tuning factor in (64)).

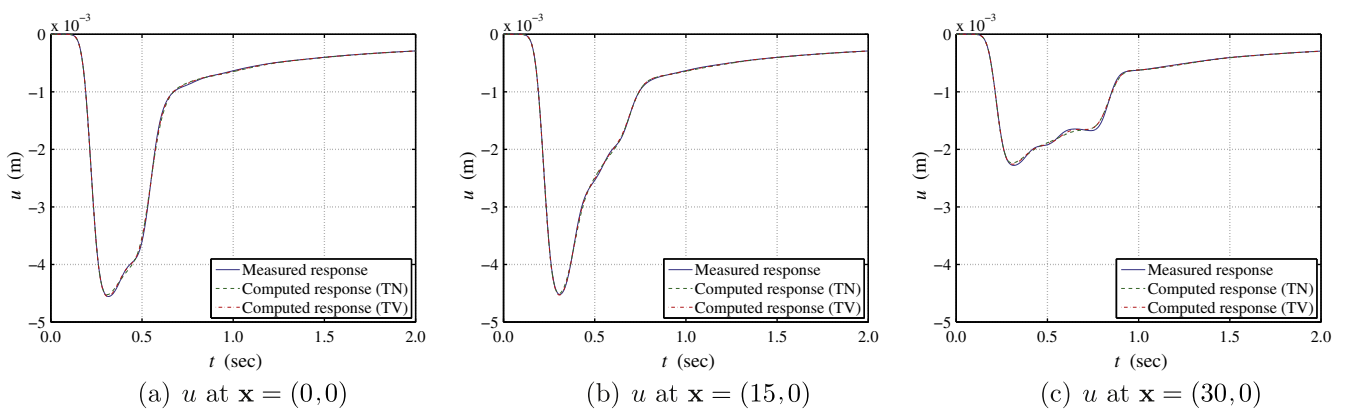


Fig. 9. Comparison of the measured and computed responses; the latter responses are obtained by solving the forward problem using the most recently updated shear wave velocity profile.

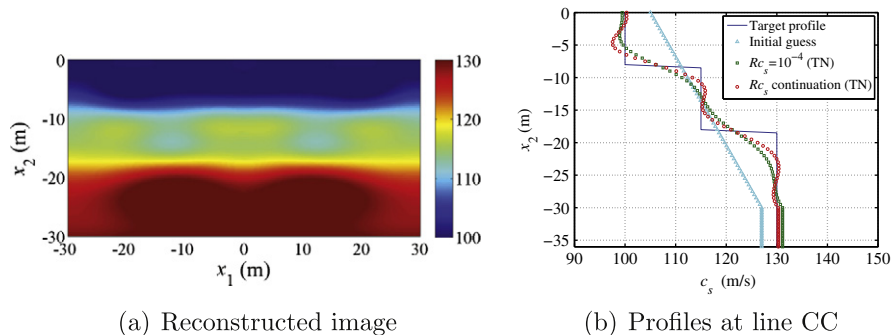


Fig. 10. Inverted 3-layer velocity profile using TN regularization with the regularization factor continuation scheme (after 2600 iterations).

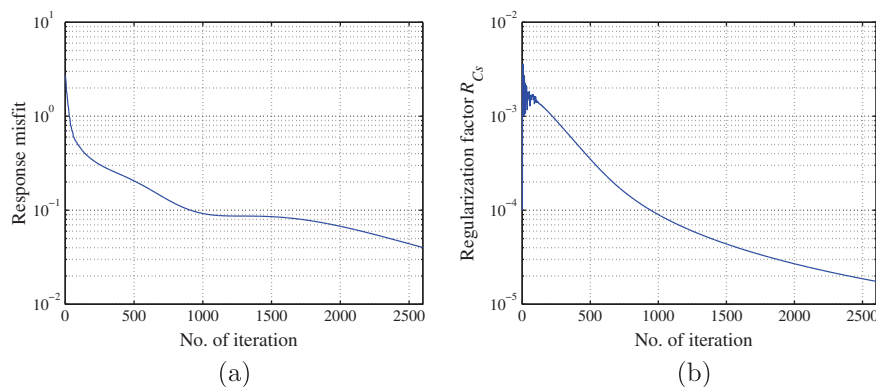


Fig. 11. (a) Misfit error \mathcal{F}_m , and (b) Regularization factor R_{c_s} , versus number of iterations; 3-layer case, with regularization factor continuation scheme.

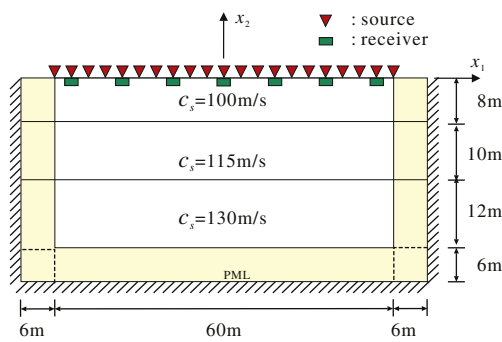


Fig. 12. Configuration of distributed sources and 7 receivers to probe the 3-layer profile.

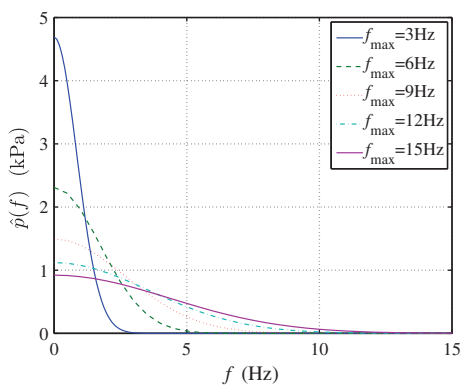


Fig. 13. Frequency spectra of the Gaussian pulse-type signals with increasingly higher frequencies (maximum frequency $f_{\max} = 3, 6, 9, 12,$ and 15 Hz).

Next, we reduce the number of sources and/or receivers on the surface. In this case, however, the target profile is harder to reconstruct, since there is less information than in the case of using distributed sources and receivers. As a result, the solution multiplicity problem becomes more pronounced. To alleviate the difficulty, we use a source-frequency continuation scheme to generate a sequence of solutions that remain, hopefully, in the basin of attraction of the global minimum. We consider Gaussian pulse-type

loads with maximum frequencies of $f_{\max} = 3, 6, 9, 12,$ and 15 Hz, respectively, which we use in sequence to probe the domain. Specifically, starting from the lowest frequency, we let the algorithm converge to a profile. We then feed the converged profile as initial guess when the domain is probed by the next higher frequency, and we repeat the process until all probing frequencies are exhausted. Fig. 13 shows the frequency spectrum of the Gaussian pulse loads, exhibiting a peak amplitude of 10,000 Pa. Total load duration is 3 s when $f_{\max} = 3$ Hz, and 2 s for all other cases.

First, we consider distributed sources and 7 receivers spaced at 9 m intervals, as shown in Fig. 12. The target is again the 3-layer profile of Fig. 3. We start the inversion with a homogeneous initial guess of $c_s = 110$ m/s. Fig. 14 shows a series of inverted 3-layer velocity profiles, each corresponding to a different frequency. We note that the lower frequencies result in a rough delineation of the layers, having, in fact, missed the middle layer, which is, nevertheless, recovered when higher frequencies are used for probing. Fig. 15 shows the variation of the misfit and the regularization factor for each source frequency. For all frequency cases, we used TV regularization endowed with the regularization factor continuation scheme.

Next, we consider distributed sources and 3 receivers at 18 m intervals, as shown in Fig. 16(a). Fig. 16(b) shows the reconstructed 3-layer profile, where again we started from a homogeneous initial guess of $c_s = 110$ m/s. The target profile of Fig. 3(b) is delineated fairly well, but the quality is worse when compared to the image obtained using 7 receivers (Fig. 14(f)), as expected.

Next, we reduce the number of sources as well. We apply Gaussian pulse loads on 7 and 1 locations on the surface, respectively, and collect responses at 7 receiver locations (all equispaced). Fig. 17 shows the reconstructed velocity profiles for each case. Again, the initial guess is a homogeneous 110 m/s, and both the source frequency and the regularization factor continuation schemes have been applied. As can be seen in the figure, the recovered profiles get progressively worse as fewer sources are used, which, in turn, result in partial domain illumination.

5.2. 5-layer problems

Next, we look into the inversion of more complicated shear wave velocity profiles including layers with an inclusion, curved layers, and a layered profile involving a soft intermediate layer. First, we consider a profile with 5 horizontal layers, as depicted

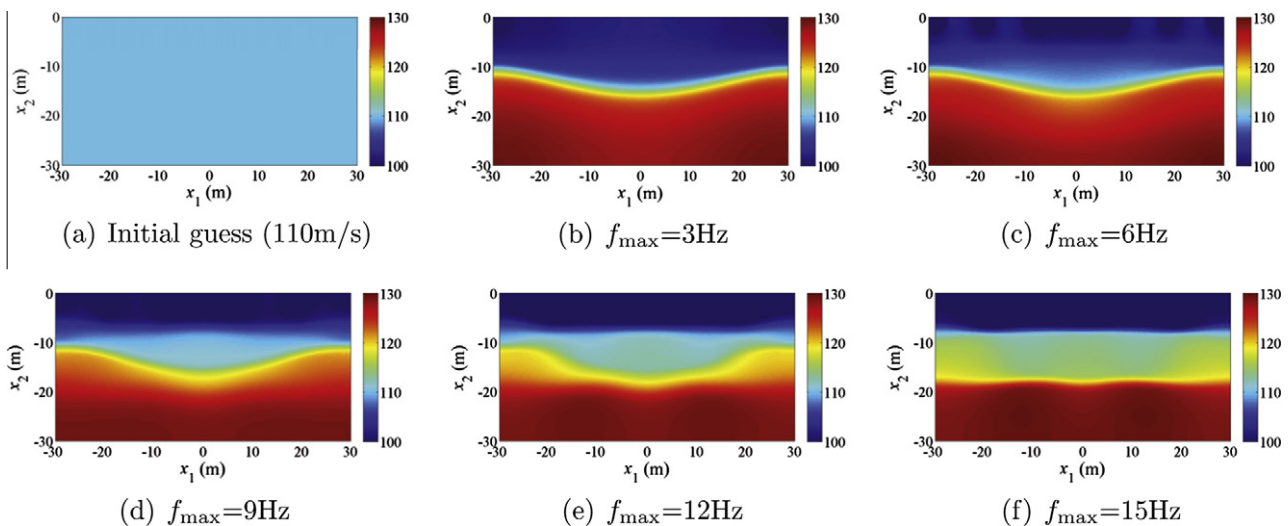


Fig. 14. Initial guess and inverted 3-layer velocity profiles corresponding to successively increasing source frequencies; distributed sources and 7 receivers are used.

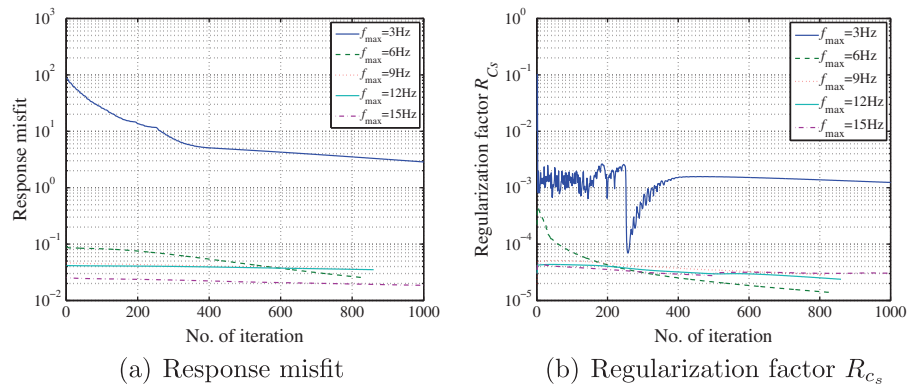


Fig. 15. (a) Response misfit \mathcal{F}_m , and (b) Regularization factor R_{C_s} versus number of iterations; source-frequency continuation scheme; distributed sources and 7 receivers are used.

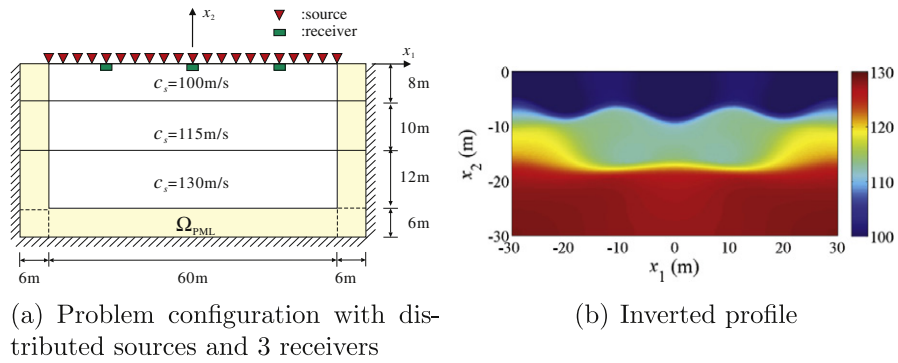


Fig. 16. Inversion for the 3-layer shear wave velocity profile using distributed sources and 3 receivers.

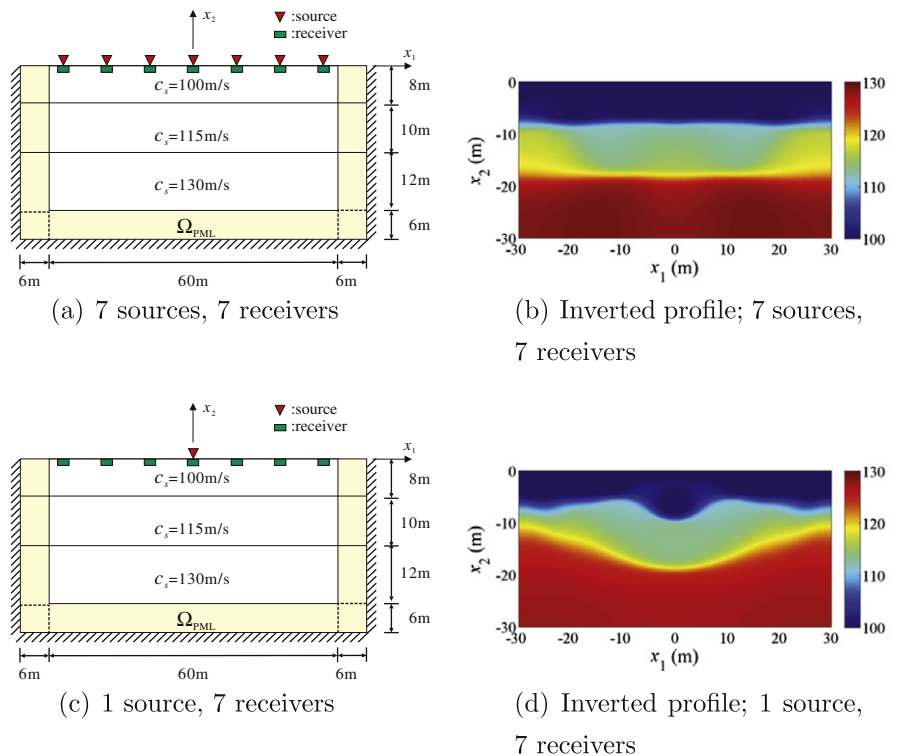


Fig. 17. Inversion for the 3-layer shear wave velocity profile using fewer sources and receivers; source frequency and regularization factor continuation schemes have been used.

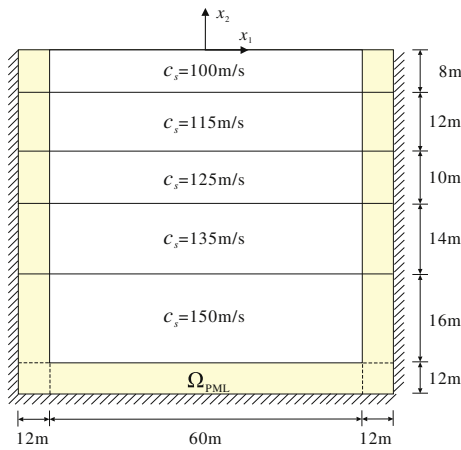


Fig. 18. A PML-truncated heterogeneous half-plane with 5 layers.

in Fig. 18. The size of the regular domain is now 60×60 m, where 12 m-wide PMLs are introduced on its sides and bottom. The layer velocities are 100, 115, 125, 135, and 150 m/s from top to bottom, while the density is 2000 kg/m^3 for all 5 layers. Both regular and PML domains are discretized by using biquadratic square elements (1×1 m). Again, the reflection coefficient is set to $|R| = 10^{-8}$. The total load duration is 4s for $f_{\max} = 3$ Hz, 3 s for $f_{\max} = 6, 9$ Hz, and

2.5 s for $f_{\max} = 12, 15$ Hz. We use distributed sources and receivers on the entire surface of the domain. Fig. 19 depicts the 5-layer velocity profile as it was successfully reconstructed using TV regularization. The target and inverted velocity profiles are plotted together over the vertical cross-section at $x_1 = 10$ m, where a fairly good match can be seen. In Fig. 20, the target 5-layer profile has an elliptical inclusion with $c_s = 150$ m/s. The inclusion is detected quite well, exposing the value of c_s as well as its location and shape. In Fig. 21, the target layers are curved with the same c_s distribution as in Fig. 18. The inverted profile reveals the curved layers and the value of c_s excellently. In Fig. 22, the third layer of the target is relatively softer than the surrounding layers. The value of c_s and the location and depth of each layer is disclosed satisfactorily in this case as well. For all the examples, the initial guess is homogeneous with $c_s = 110$ m/s, and both the source frequency and the regularization factor continuation schemes have been utilized.

5.3. Noise effect

Next, we investigate the effect of noise on the quality of the inverted profiles. To this end, we inject 20% Gaussian noise to the noise-free data obtained for the 5-layer velocity profile shown in Fig. 18. We apply the same Gaussian pulse-type loads, with the frequency spectra depicted in Fig. 13. Fig. 23 shows the noise-polluted displacement responses at three locations on the surface ($x_1 = 0, 15,$ and 30 m) for the load with $f_{\max} = 15$ Hz. Fig. 24(b) shows the reconstructed image using TV regularization. In Fig. 24(c), the

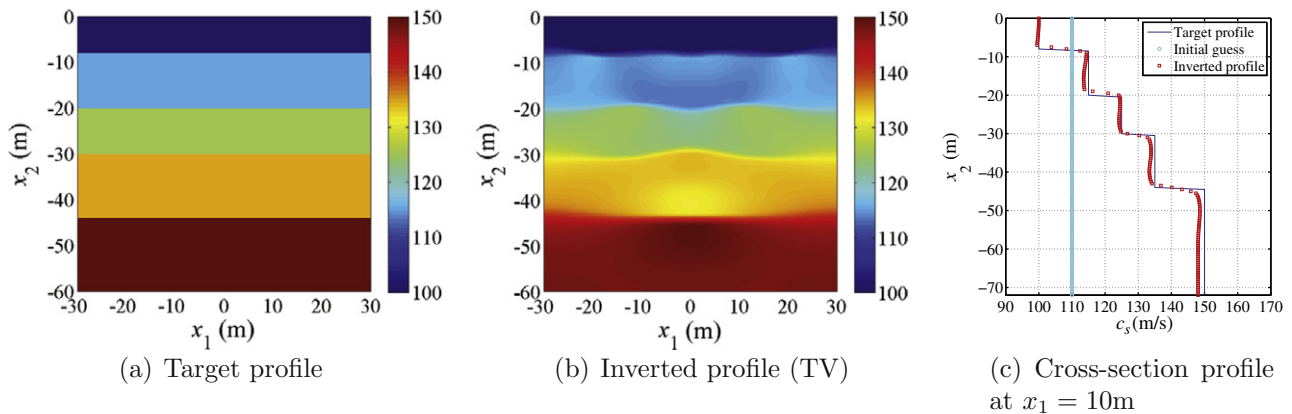


Fig. 19. Target and inverted shear wave velocity profiles; 5 layers.

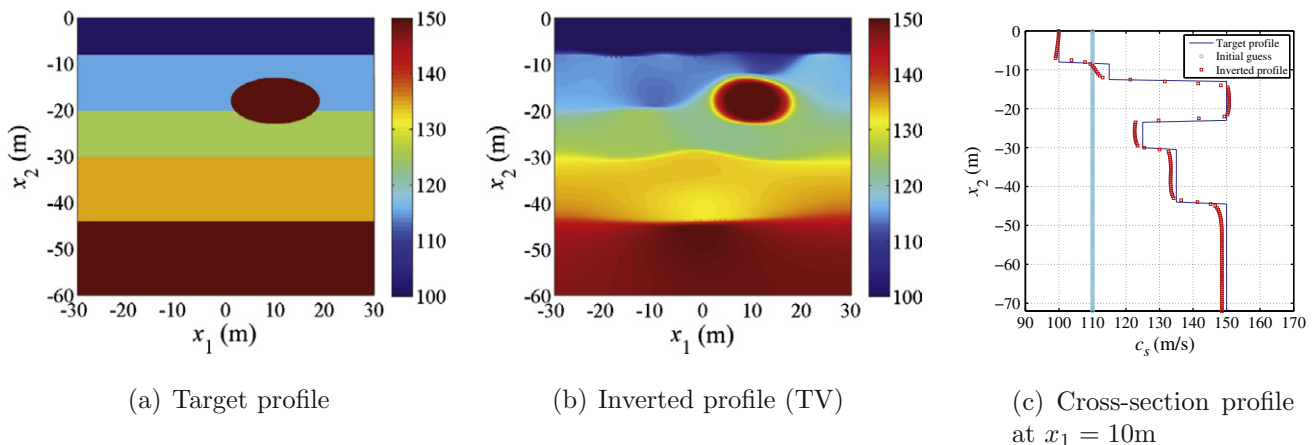


Fig. 20. Target and inverted shear wave velocity profiles; 5 layers and inclusion.

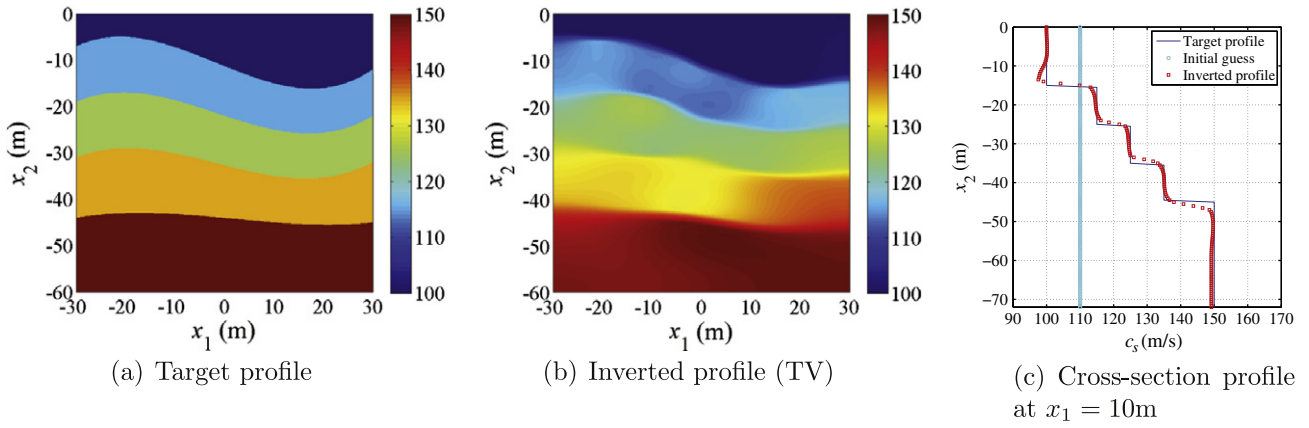


Fig. 21. Target and inverted shear wave velocity profiles; 5 curved layers.

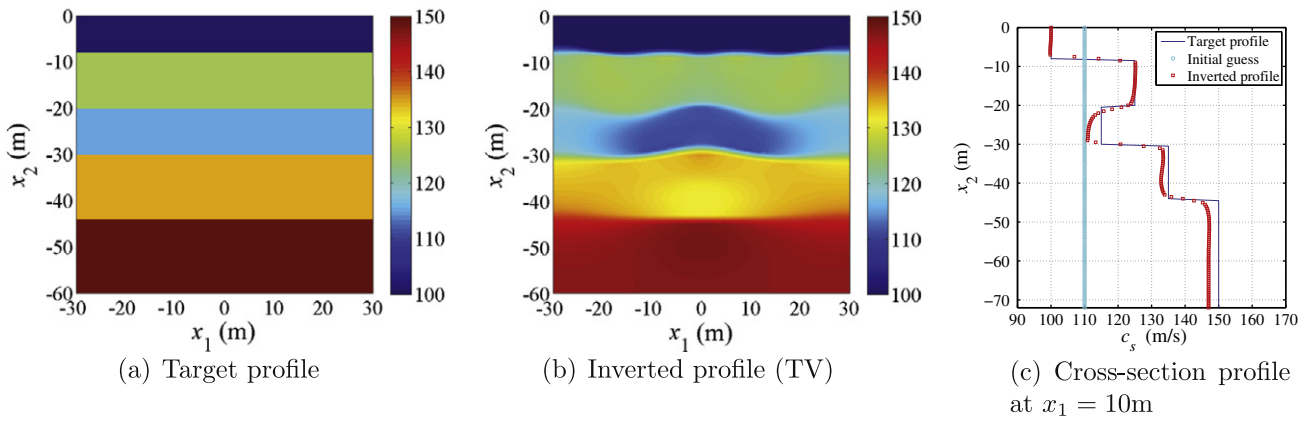


Fig. 22. Target and inverted shear wave velocity profiles; 5 horizontal layers with a soft material in the third layer.

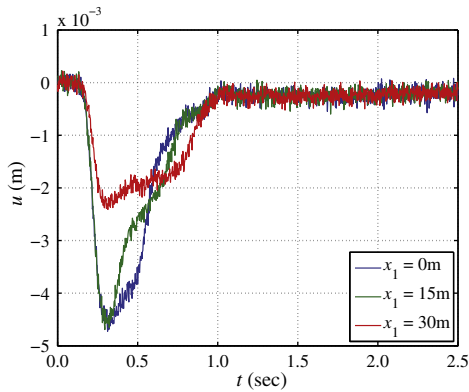


Fig. 23. Measured displacement responses at three surface locations ($x_1 = 0, 15,$ and 30 m) with 20% Gaussian noise.

inverted profiles for both noisy and noise-free data are plotted together along the vertical cross-section at $x_1 = 10$ m. As seen in the figure, the inverted profile derived from the noisy data has degraded somewhat when compared to the noise-free result (Fig. 24(c)). Nevertheless, the recovered profile is still quite acceptable.

5.4. Inversion by the weak form of the reduced gradient

Thus far, we have described the inversion process based on a gradient scheme for updating the material properties, where the

reduced gradient (54) was used to drive the gradient scheme. Condition (26) was imposed explicitly. In lieu, though, of the strong form of the reduced gradient (54), a weak form could also be used. The advantage is that condition (26) will be automatically taken into account. We illustrate using (27) as the starting point. We multiply (27) by a test function $w(\mathbf{x})$ and integrate over the entire domain Ω to get:

$$R_{c_s} \int_{\Omega} \nabla w \cdot \nabla c_s d\Omega - 2 \int_{\Omega} w c_s \left[\int_0^T \lambda_s \cdot \nabla \left(\frac{\partial v}{\partial t} \right) dt \right] d\Omega = 0, \quad \text{in } \Omega, \quad (65)$$

where the first term results from integration by parts while also taking into account the boundary condition $\partial c_s / \partial n = 0$ (Eq. (26)). Introducing quadratic approximant ϕ_i for both $w(\mathbf{x})$ and $c_s(\mathbf{x})$ results in a discrete reduced gradient of the following form:

$$\mathbf{g} = \mathbf{K} \mathbf{c}_s = (R_{c_s} \mathbf{K}_r + \mathbf{K}_s) \mathbf{c}_s, \quad (66)$$

where

$$(\mathbf{K}_r)_{ij} = \int_{\Omega} \left(\frac{\partial \phi_i}{\partial x_1} \frac{\partial \phi_j}{\partial x_1} + \frac{\partial \phi_i}{\partial x_2} \frac{\partial \phi_j}{\partial x_2} \right) d\Omega, \quad (67a)$$

$$(\mathbf{K}_s)_{ij} = -2 \int_{\Omega} \phi_i \phi_j \left[\int_0^T \lambda_s \cdot \nabla \left(\frac{\partial v}{\partial t} \right) dt \right] d\Omega. \quad (67b)$$

In (66), $\mathbf{K}_r \mathbf{c}_s$ and $\mathbf{K}_s \mathbf{c}_s$ correspond to the gradient of the regularization functional ($\nabla_{c_s} \mathcal{F}_r$) and the gradient of the side-imposed functional ($\nabla_{c_s} \mathcal{F}_s$), respectively. In Fig. 25, we show the reconstructed 5-layer profile obtained by exploiting the weak form of the reduced gradient. The image recovers well the 5-layer velocity profile, but is

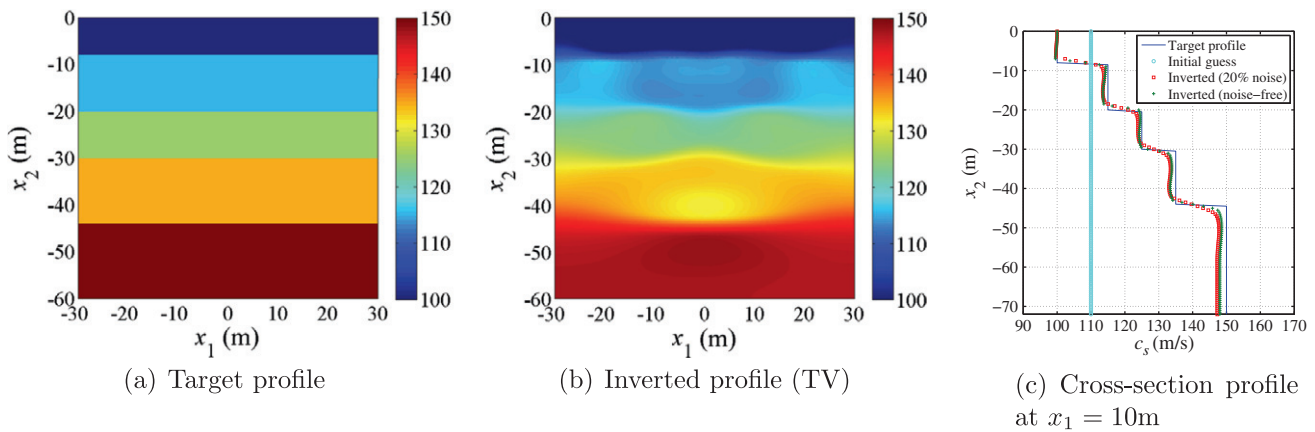


Fig. 24. Inverted 5-layer velocity profiles using measured data with 20% Gaussian noise.

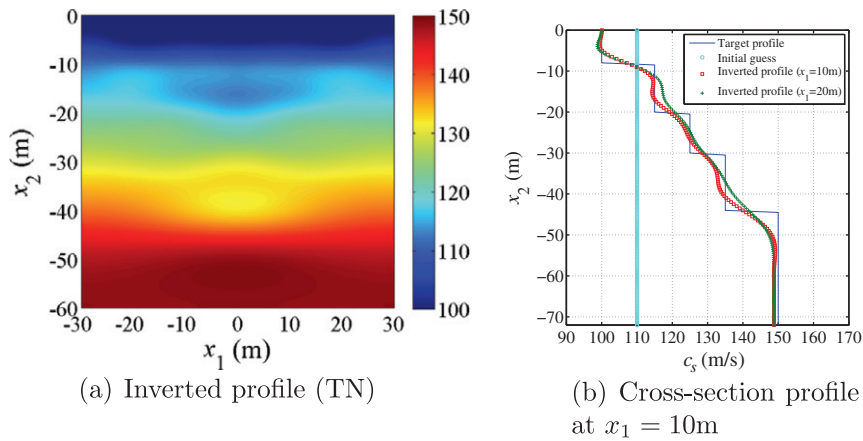


Fig. 25. Inverted 5-layer shear wave velocity profile using the weak form of the reduced gradient; TN regularization is used.

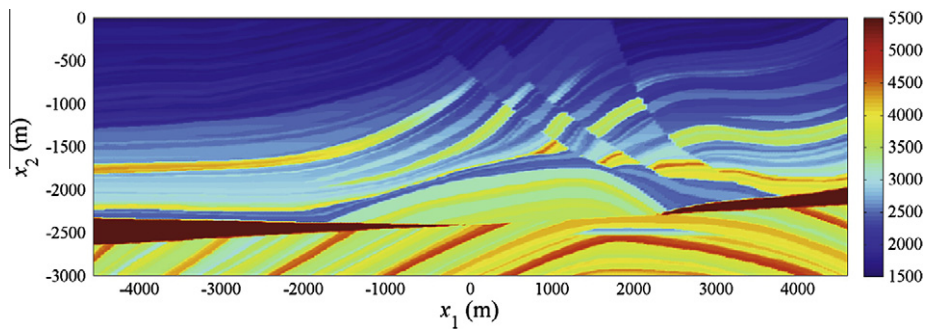


Fig. 26. The Marmousi velocity model.

of lesser quality when compared to Fig. 19(b): we attribute this primarily to our use of the TN regularization in this case. In general, there are two advantages for choosing the weak form over the strong form: firstly, there is no need to calculate the Laplacian (Δc_s), whose numerical evaluation causes difficulties.⁴ Secondly, the Neumann-type boundary condition (26) is automatically satisfied

in the weak form, so that there is no need to explicitly impose the condition. On the other hand, the weak form of the reduced gradient requires the assembly of \mathbf{K}_s at every inversion iteration, causing additional computational cost.

5.5. The Marmousi benchmark model

Lastly, we use the PML-endowed full waveform inversion process to reconstruct the Marmousi profile, a highly-heterogeneous benchmark problem proposed in the oil-exploration community [40]. The Marmousi model was created by the Institut Français du Pétrole (IFP) in 1988, and has become an industry standard after

⁴ The material properties c_s are interpolated using C^0 elements, and, therefore, their second spatial derivatives behave as Dirac functions. Thus, the finite difference stencil we use for approximating the Laplacian at nodal locations could lead to errors, particularly for elements whose sides form larger angles with the coordinate axes. In the numerical examples reported herein, highly distorted meshes were avoided.

the 1990 EAEG workshop on practical aspects of seismic data inversion. Fig. 26 shows the target Marmousi velocity profile. It contains 158 layers and is 9.2 km in length and 3 km in depth, respectively. The density is 2200 kg/m³. We place PMLs (288 m wide) along the sides and bottom of the domain and discretize the combined regular and PML domains using biquadratic elements. The element size is 80 × 24 m in the regular domain and 24 × 24 m in the PML regions. We use a stress shot $\sigma_{32} = p(t)$ at every grid point on the entire surface of the regular domain, as is typically done [29,18,19]. We use Gaussian pulse-type loads with two different maximum frequencies; $f_{\max} = 10$ and 40 Hz. The time steps used are 0.006 and 0.0018 s for each frequency signal. Sensor readings of the anti-plane displacement are synthesized at all grid points on the surface. Fig. 27 shows the synthetic seismograms

generated for the Marmousi profile using the two Gaussian pulse-type loads.

We started the inversion process with a linear profile varying from 1500 to 4500 m/s in depth. We used both TN and TV regularization schemes. By using, first, the signal with $f_{\max} = 10$ Hz, the Marmousi velocity model is reconstructed as shown in Fig. 28. The converged profiles recovered the velocity structure of the shallow subsurface fairly well, exposing the location and dip of the strata. Then, we provide the inverted profiles of Fig. 28 as a new initial guess to a subsequent inversion using the higher-frequency signal of $f_{\max} = 40$ Hz. There result the updated velocity profiles depicted in Fig. 29. Reflectors, steep dips, and strong velocity gradients in both vertical and lateral directions are captured satisfactorily, although it is difficult to obtain a precise image of the deeper parts

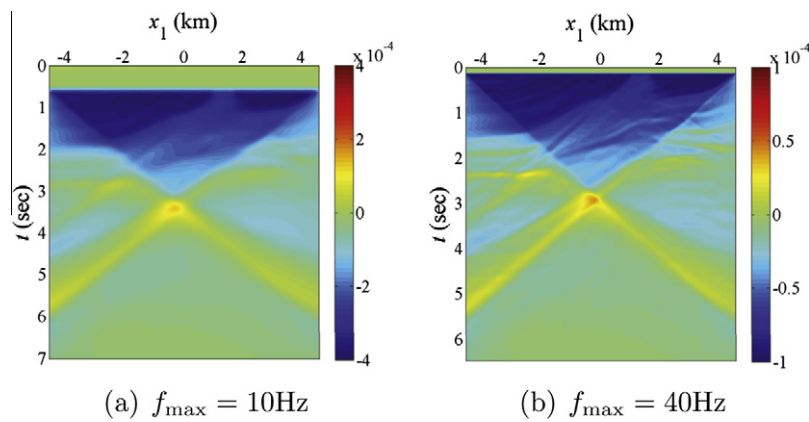


Fig. 27. Synthetic seismograms generated for the Marmousi model using Gaussian pulse-type loads with maximum frequencies $f_{\max} = 10$ and 40 Hz.

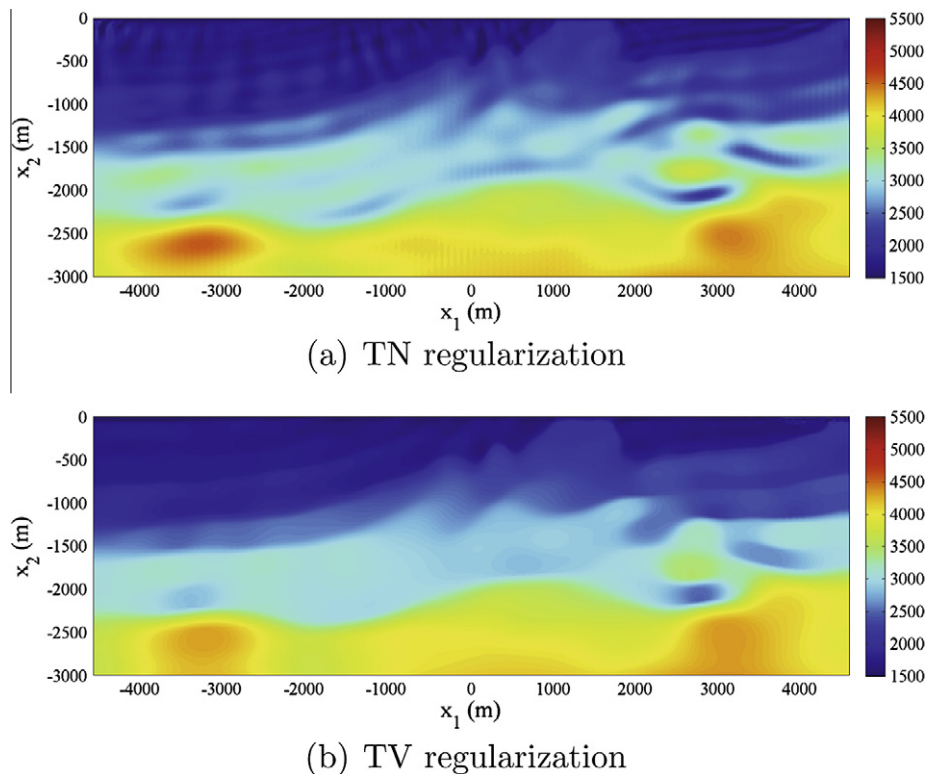


Fig. 28. Reconstructed Marmousi velocity profile using a Gaussian pulse with $f_{\max} = 10$ Hz.

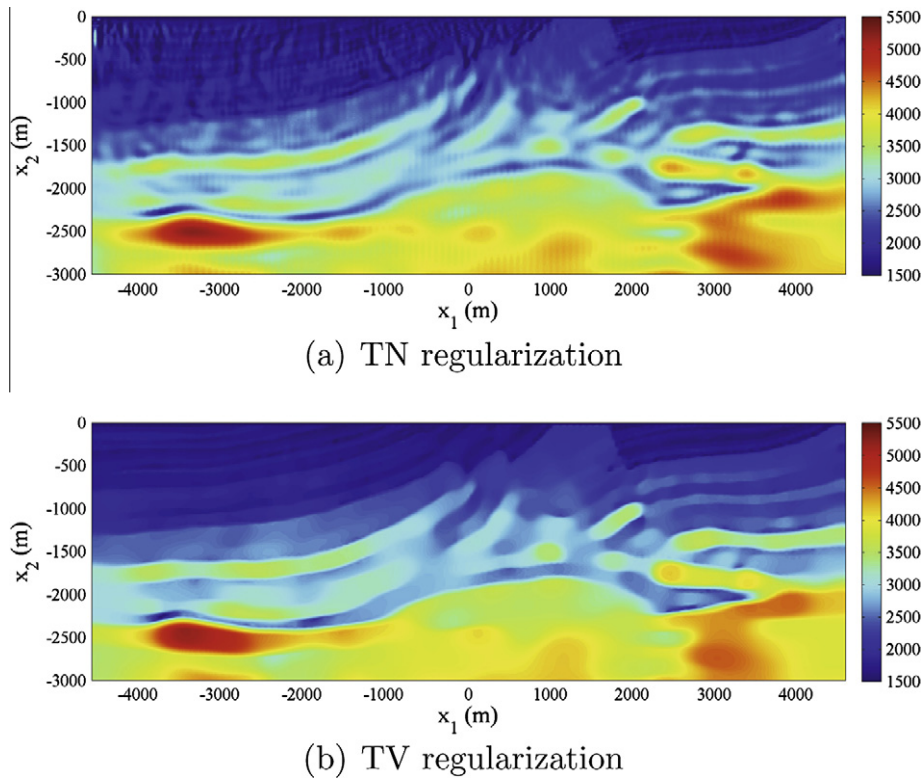


Fig. 29. Reconstructed Marmousi velocity profile using a Gaussian pulse with $f_{\max} = 40$ Hz.

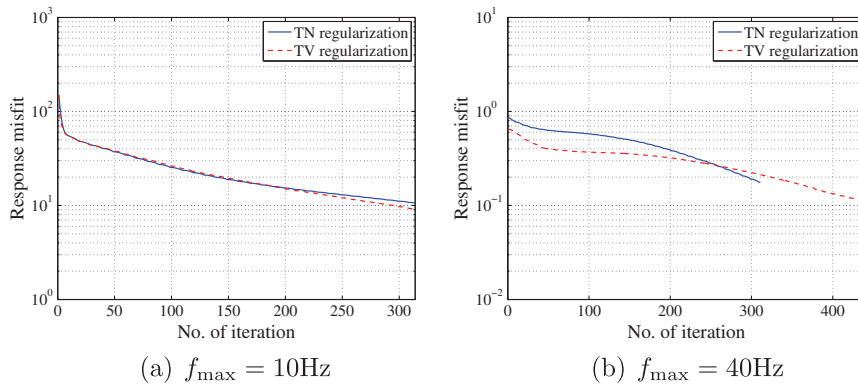


Fig. 30. Response misfit versus number of iterations for the Marmousi model.

of the domain below the salt dome. Fig. 30 depicts the histories of the misfit functional \mathcal{F}_m for both source-frequency cases.

We remark that most published attempts to invert for the Marmousi profile are carried out in the frequency-domain (e.g. [18,19,44,45]) using, at least, tens of probing frequencies. The recovery of the deeper part of the profile, remains a challenge, even when several frequencies are used. To the best of our knowledge, direct time-domain inversion, which here was executed using only two pulses, while simultaneously the domain is truncated using absorbing boundaries (PMLs) appropriate for heterogeneous media, is attempted here for the first time.

6. Conclusions

We discussed a full waveform inversion approach for reconstructing the shear wave velocity profile of a two-dimensional heterogeneous semi-infinite medium, truncated by a perfectly-

matched-layer (PML), based on surface measurements of its response to surface excitation. The PML was introduced to accommodate the truncation of the semi-infinite extent and absorb the outgoing waves traveling beyond the truncation interface. The underlying numerical scheme was based on a new displacement-stress mixed finite-element formulation in the time-domain developed recently [11].

The PML-endowed PDEs are used within a PDE-constrained optimization framework to resolve the inverse medium problem. In order to alleviate the inherent ill-posedness of the inverse problem, we explored both Tikhonov (TN) and total variation (TV) regularization. Both schemes captured target profiles efficiently. For sharply-varying profiles, the TN scheme exhibited limitations when the regularization factor was large and not allowed to vary, whereas the TV scheme showed good performance. To improve on the ability to recover sharp profiles, we suggested a regularization factor continuation scheme, which tunes the regularization factor at each inversion

iteration. The continuation scheme works quite effectively in recovering sharp profiles even when the regularization factor is initially large. We also employed a source-frequency continuation scheme to generate a sequence of solutions that remain in the basin of attraction of the global minimum. The two continuation schemes greatly aid in recovering target profiles when there are fewer sources and receivers. We used both noise-free and noisy data to demonstrate the algorithmic performance, and showed robustness of the full waveform inversion in the presence of noise in the measured data. We also discussed two different ways of implementing the reduced gradient that drives material updates. We discussed several numerical results, including the Marmousi benchmark problem. The highly heterogeneous velocity structure of the Marmousi model has been recovered reasonably well, demonstrating the applicability of the PML-endowed full waveform inversion to problems ranging from geotechnical site characterization to geophysical probing applications of industrial interest.

Acknowledgment

Partial support for the authors research has been provided by the National Science Foundation under grant award CMMI-0348484. This support is gratefully acknowledged.

Appendix A. Gaussian pulse expressions

The various Gaussian pulses used in the numerical experiments for domain probing have the following expressions:

$$\begin{aligned}
 f_{\max} = 3 \text{ Hz} : \quad p(t) &= -10 \exp \left[-\frac{(t - 0.8)^2}{0.07} \right], \\
 f_{\max} = 6 \text{ Hz} : \quad p(t) &= -10 \exp \left[-\frac{(t - 0.45)^2}{0.017} \right], \\
 f_{\max} = 9 \text{ Hz} : \quad p(t) &= -10 \exp \left[-\frac{(t - 0.35)^2}{0.0071} \right], \\
 f_{\max} = 12 \text{ Hz} : \quad p(t) &= -10 \exp \left[-\frac{(t - 0.26)^2}{0.004} \right], \\
 f_{\max} = 15 \text{ Hz} : \quad p(t) &= -10 \exp \left[-\frac{(t - 0.22)^2}{0.0027} \right]. \quad (68)
 \end{aligned}$$

where f_{\max} denotes the maximum frequency present in the Fourier Transform of the corresponding pulse.

References

- [1] W. Chew, Q. Liu, Perfectly matched layers for elastodynamics: a new absorbing boundary condition, *J. Comput. Acoust.* 4 (4) (1996) 341–359.
- [2] F. Collino, C. Tsogka, Application of the perfectly matched absorbing layer model to the linear elastodynamic problem in anisotropic heterogeneous media, *Geophysics* 66 (1) (2001) 294–307.
- [3] B. Engquist, A. Majda, Absorbing boundary conditions for the numerical simulation of waves, *Math. Comput.* 31 (139) (1977) 629–651.
- [4] R. Higdon, Absorbing boundary conditions for elastic waves, *Geophysics* 56 (2) (1991) 231–241.
- [5] L. Kallivokas, S. Lee, Local absorbing boundaries of elliptical shape for scalar waves, *Comput. Meth. Appl. Mech. Engrg.* 193 (2004) 4979–5015.
- [6] D. Givoli, J. Keller, A finite element method for large domains, *Comput. Meth. Appl. Mech. Engrg.* 76 (1989) 41–66.
- [7] D. Givoli, J. Keller, Non-reflecting boundary conditions for elastic waves, *Wave Motion* 12 (3) (1990) 261–279.
- [8] Y. Zheng, X. Huang, Anisotropic perfectly matched layers for elastic waves in cartesian and curvilinear coordinates, Earth Research Laboratory Report, Massachusetts Institute of Technology, Cambridge, 2002.
- [9] U. Basu, A.K. Chopra, Perfectly matched layers for time-harmonic elastodynamics of unbounded domains: theory and finite-element implementation, *Comput. Meth. Appl. Mech. Engrg.* 192 (2003) 1337–1375.
- [10] U. Basu, A.K. Chopra, Perfectly matched layers for transient elastodynamics of unbounded domains, *Int. J. Numer. Meth. Engrg.* 59 (2004) 1039–1074.
- [11] J.W. Kang, L.F. Kallivokas, Mixed unsplit-field perfectly-matched-layers for transient simulations of scalar waves in heterogeneous domains, *Comput. Geosci.* 14 (4) (2010) 623–648.
- [12] F. Hastings, J. Schneider, S. Broschat, Application of the perfectly matched layer (PML) absorbing boundary condition to elastic wave propagation, *J. Acoust. Soc. Am.* 100 (5) (1996) 3061–3069.
- [13] R.M. Shipp, S.C. Singh, Two-dimensional full wavefield inversion of wide-aperture marine seismic streamer data, *Geophys. J. Int.* 151 (2) (2002) 325–344.
- [14] L. Sirgue, R.G. Pratt, Efficient waveform inversion and imaging: a strategy for selecting temporal frequencies, *Geophysics* 69 (1) (2004) 231–248.
- [15] S. Operto, C. Ravaut, L. Improta, J. Virieux, A. Herrero, P. Dell'Aversana, Quantitative imaging of complex structures from dense wide-aperture seismic data by multiscale traveltimes and waveform inversions: a case study, *Geophys. Prospect.* 52 (6) (2004) 625–651.
- [16] R.G. Pratt, R.M. Shipp, Seismic waveform inversion in the frequency domain, part 2: fault delineation in sediments using crosshole data, *Geophysics* 64 (3) (1999) 902–914.
- [17] F. Gao, A. Levander, R.G. Pratt, C.A. Zelt, G.-L. Fradelizio, Waveform tomography at a groundwater contamination site: surface reflection data, *Geophysics* 72 (2007) G45–G55.
- [18] Y. Choi, C. Shin, D. Min, T. Ha, Efficient calculation of the steepest descent direction for source-independent seismic waveform inversion: an amplitude approach, *J. Comput. Phys.* 208 (2005) 455–468.
- [19] Y. Choi, D. Min, C. Shin, Frequency-domain elastic full waveform inversion using the new pseudo-Hessian matrix – experience of elastic Marmousi-2 synthetic data, *Bull. Seismol. Soc. Am.* 98 (5) (2008) 2402–2415.
- [20] P. Chen, L. Zhao, T.H. Jordan, Full 3D tomography for the crustal structure of the Los Angeles region, *Bull. Seismol. Soc. Am.* 97 (2007) 1094–1120.
- [21] I. Epanomeritakis, V. Akcelik, O. Ghattas, J. Bielak, A Newton-CG method for large-scale three-dimensional elastic full-waveform seismic inversion, *Inverse Probl.* 24 (2008) 034015, doi:10.1088/0266-5611/24/3034015.
- [22] V. Akcelik, G. Biros, O. Ghattas, Parallel multiscale Gauss–Newton–Krylov methods for inverse wave propagation, in: *Proceedings of the Supercomputing 2002*, Baltimore, 2002.
- [23] V. Akcelik, J. Bielak, G. Biros, I. Epanomeritakis, A. Fernandez, O. Ghattas, E.J. Kim, J. Lopez, D.R. O'Hallaron, T. Tu, J. Urbanic, High resolution forward and inverse earthquake modeling on terascale computers, in: *Proceedings of the Supercomputing 2003*, Phoenix, AZ, 2003.
- [24] A. Askan, V. Akcelik, J. Bielak, O. Ghattas, Full waveform inversion for seismic velocity and anelastic losses in heterogeneous structures, *Bull. Seismol. Soc. Am.* 97 (6) (2007) 1990–2008.
- [25] A. Askan, J. Bielak, Anelastic waveform tomography including model uncertainty, *Bull. Seismol. Soc. Am.* 98 (6) (2008) 2975–2989.
- [26] G. Chavent, F. Clément, S. Gómez, Waveform inversion by MBTT formulation, in: *Proceedings of the 3rd International Conference on Mathematical and Numerical Aspects of Wave Propagation*, SIAM, Philadelphia, 713–722, 1995.
- [27] G. Chavent, C.A. Jacewitz, Determination of background velocities by multiple migration fitting, *Geophysics* 60 (2) (1995) 476–490.
- [28] R.-E. Plessix, Y.-H. De Roeck, G. Chavent, Waveform inversion of reflection seismic data for kinematic parameters by local optimization, *SIAM J. Sci. Comput.* 20 (3) (1999) 1033–1052.
- [29] C. Bunks, F.M. Saleck, S. Zaleski, G. Chavent, Multiscale seismic waveform inversion, *Geophysics* 60 (5) (1995) 1457–1473.
- [30] A. Tikhonov, Solution of incorrectly formulated problems and the regularization method, *Soviet Math. Doklady* 4 (1963) 1035–1038.
- [31] R. Acar, C.R. Vogel, Analysis of bounded variation penalty methods for ill-posed problems, *Inverse Probl.* 10 (1994) 1217–1229.
- [32] G.F. Carey, J.T. Oden, *Finite Elements – A Second Course*, vol. II, Prentice-Hall, 1983.
- [33] F. Brezzi, M. Fortin, *Mixed and Hybrid Finite Element Methods*, Springer-Verlag, New York, NY, 1991.
- [34] K. Bathe, *Finite Element Procedures*, Prentice-Hall, Englewood Cliffs, NJ, 1996.
- [35] S. Rao, *Engineering Optimization: Theory and Practice*, John Wiley and Sons, Inc., 1996.
- [36] J. Nocedal, S. Wright, *Numerical Optimization*, Springer, 1999.
- [37] P. Hansen, D. O'Leary, The use of the L -curve in the regularization of discrete ill-posed problems, *SIAM J. Sci. Comput.* 14 (6) (1993) 1487–1503.
- [38] P. McCarthy, Direct analytic model of the L -curve for Tikhonov regularization parameter selection, *Inverse Probl.* 19 (2003) 643–663.
- [40] R. Versteeg, The Marmousi experience: velocity model determination on a synthetic complex data set, *The Leading Edge* 13 (1994) 927–936.
- [41] S.-W. Na, L.F. Kallivokas, Continuation schemes for shape detection in inverse acoustic scattering problems, *Comput. Model. Engrg. Sci.* 35 (1) (2008) 73–90.
- [42] W.W. Symes, Migration velocity analysis and waveform inversion, *Geophys. Prospect.* 56 (6) (2008) 765–790.
- [43] R.-E. Plessix, Introduction: towards a full waveform inversion, *Geophys. Prospect.* 56 (6) (2008) 761–763.
- [44] A. Abubakar, W. Hu, T.M. Habashy, P.M. Berg, Application of the finite-difference contrast-source inversion algorithm to seismic full-waveform data, *Geophysics* 74 (6) (2009) WCC47–WCC58.
- [45] W.A. Mulder, R.-E. Plessix, Exploring some issues in acoustic full waveform inversion, *Geophys. Prospect.* 56 (2008) 827–841.